ИЗВЕСТИЯ ВЫСШИХ УЧЕБНЫХ ЗАВЕДЕНИЙ.
Т 60 (6) Серия «**ХИМИЯ И ХИМИЧЕСКАЯ ТЕХНОЛОГИЯ**» 2017

IZVESTIYA VYSSHIKH UCHEBNYKH ZAVEDENIY
V 60 (6) **KHIMIYA KHIMICHESKAYA TEKHNOLOGIYA** 2017
RUSSIAN JOURNAL OF CHEMISTRY AND CHEMICAL TECHNOLOGY

DOI: 10.6060/tcct.2017606.5609

УДК: 544.13

СВЕРХБЫСТРАЯ ЭЛЕКТРОННАЯ КРИСТАЛЛОГРАФИЯ И НАНОКРИСТАЛЛОГРАФИЯ: ДЛЯ ХИМИИ, БИОЛОГИИ И МАТЕРИАЛОВЕДЕНИЯ. ЧАСТЬ II. СВЕРХБЫСТРАЯ ЭЛЕКТРОННАЯ НАНОКРИСТАЛЛОГРАФИЯ

Л. Шефер, Ю.И. Тарасов, Н.В. Шаронова, А.А. Ищенко

Лотар Шефер

Университет штата Арканзас, 727008 Фейетвилл, Арканзас, США
E-mail: schafer@uark.edu

Юрий Игоревич Тарасов

Кафедра физики и технической механики, Институт тонких химических технологий, Московский технологический университет, просп. Вернадского, 86, Москва, Российская Федерация, 119571,
Объединенный институт высоких температур РАН, Москва, ул. Ижорская, 13, стр. 2, 125412
E-mail: y.i.tarasov@mitht.org

Нина Валерьевна Шаронова, Анатолий Александрович Ищенко *

Кафедра аналитической химии, Институт тонких химических технологий, Московский технологический университет, просп. Вернадского, 86, Москва, Российская Федерация, 119571
E-mail: ninokk2008@yandex.ru, aischenko@yasenevo.ru *

В статье описан метод сверхбыстрой электронной нанокристаллографии – конкретной реализации метода сверхбыстрой электронной кристаллографии, оптимизированной для высокочувствительного и высокоэффективного сбора данных при исследовании наноструктур с высоким временным разрешением, от пико до фемтосекунд. Эти достижения открыли новые возможности для изучения когерентной структурной динамики наночастиц. Наноструктуры характеризуются рядом необычных свойств по сравнению с их объемными аналогами. Прежде всего, это связано с проявлением квантово-размерного эффекта и относительно большого числа структурных единиц наночастицы, находящихся на ее поверхности. Одной из структурных особенностей является возникновение так называемых нанокристаллических структурных типов, которые имеют тенденцию к образованию замкнутых оболочек, и связаны с появлением магических чисел в распределении размеров. Морфология и параметры решетки нанокристаллов сильно зависят от подложки и модификации поверхности, что приводит к сжатию и образованию границ двойников из-за релаксации поверхностных деформаций. Статья описывает эксперимент сверхбыстрой электронной нанокристаллографии, теорию метода и анализ данных, а также процедуру пробоподготовки поверхности подложки и образцов при исследовании методом UEnC. Представленные примеры включают результаты изучения структурной динамики конденсированной фазы, поверхностей и нанокристаллов, динамики плавления наночастиц и прямое наблюдение генерации когерентных оптических фононов в нанопленках. В статье цитируются результаты нескольких всемирно известных исследовательских групп.

Ключевые слова: сверхбыстрая электронная нанокристаллография, переходные неравновесные структуры, когерентная структурная динамика, поверхности, наночастицы, нано-кристаллографические структуры, наноматериалы

UDC: 544.13

ULTRAFAST ELECTRON CRYSTALLOGRAPHY AND NANOCRYSTALLOGRAPHY: FOR CHEMISTRY, BIOLOGY AND MATERIALS SCIENCE. PART II. ULTRAFAST ELECTRON NANOCRYSTALLOGRAPHY

L. Schafer, Yu.I. Tarasov, N.V. Sharonova, A.A. Ischenko

Lothar Schafer

Department of Chemistry and Biochemistry, University of Arkansas, 727008 Fayetteville, AR, USA
E-mail: schafer@uark.edu

Yury I. Tarasov

Department of Physics and Technical Mechanics, Moscow University of Technology, Institute of Fine Chemical Technologies, Moscow, 119571, Russia
Joint Institute for High Temperatures of the RAS, Moscow, 125412, Russia
E-mail: y.i.tarasov@mitht.org

Nina V. Sharonova, Anatoly A. Ischenko *

Department of Analytical Chemistry, Moscow University of Technology, Institute of Fine Chemical Technologies, Moscow, 119571, Russia
E-mail: ninokk2008@yandex.ru, aischenko@yasenevo.ru *

This article shows the development of the Ultrafast Electron Nanocrystallography (UEnC), a specific implementation of Ultrafast Electron Crystallography (UEC), optimized for high sensitivity and high data acquisition efficiency and trained on the quantitative studies of different solid nanostructures with high temporal resolution ranging from pico- to femtoseconds. These achievements have opened up new possibilities for studying the coherent structural dynamics of the nanoparticles. Nanostructures are characterized by a number of unusual properties compared to their bulk counterparts. First of all, this is due to the manifestation of the quantum-size effect and the corresponding relatively-large percentage of structural units of the nanoparticle being on its surface. One of the structural features is the emergence of the so-called nanocrystallographic structure types, which have a tendency to form closed shells and are connected with the appearance of magic numbers in the size distribution. The morphology and lattice parameters of nanocrystals are strongly dependent on the substrate and the surface modification, which results in the contraction, and the formation of twin boundaries due to the relaxation of the surface deformations. The article describes UEnC experiment, the theory and data analysis, and sample preparation. The presented examples include the investigation of the structural dynamics of condensed phase, surfaces, and nanocrystals, the melting dynamics of gold nanoparticles and direct observation of coherent optical phonons generation in nanofilms. The results of several internationally renowned research groups are included and cited.

Key words: ultrafast electron nanocrystallography, transient nonequilibrium structures, coherent structural dynamics, surfaces, nanoparticles, nano-crystallographic structure types, nanomaterials

Для цитирования:
Шефер Л., Тарасов Ю.И., Шаронова Н.В., Ищенко А.А. Сверхбыстрая электронная кристаллография и нанокристаллография: для химии, биологии и материаловедения. Часть II. Сверхбыстрая электронная нанокристаллография. *Изв. вузов. Химия и хим. технология*. 2017. Т. 60. Вып. 6. С. 4–27.

For citation:
Schafer L., Tarasov Yu.I., Sharonova N.V., Ischenko A.A. Ultrafast electron crystallography and nanocrystallography: for chemistry, biology and materials science. Part II. Ultrafast electron nanocrystallography. *Izv. Vyssh. Uchebn. Zaved. Khim. Khim. Tekhnol.* 2017. V. 60. N 6. P. 4–27.

INTRODUCTION

The ultrafast electron diffraction methods give direct information on structural changes occurring in the test object in real time, and are used at present for quantitative studies of dynamic phenomena occurring in the nanosized objects in the time interval from pico- to femtoseconds [1-17]. In recent years, there was a significant decrease in the duration of the electron bunch and a significant increase of the accelerating voltage, which allowed obtaining electronic pulses of femtosecond duration. These advances have opened new opportunities for research of coherent structural dynamics of nanomaterials with a femtosecond time resolution.

One of the important stages of nanoparticle research by the Ultrafast Electron Nanocrystallography (UEnC) method is the preparation of the matrix surface on which the studied nanoparticles are deposited [1, 4]. The high sensitivity and resolution of the UEnC method open the possibility of studying processes such as surface melting of nanoparticles, the non-equilibrium structural dynamics of phase transitions and the response of adsorbed molecules on the non-equilibrium structural changes of the surface.

Processes of reversible melting of the surface and recrystallization in the subpicosecond time scale and spatial resolution up to units picometres were studied. In ultrafast photoinduced melting processes of nanoparticles, which were carried out under non-equilibrium conditions, they determined the initial phases of lattice deformation, the non-equilibrium electron–phonon interaction and, in melting, the formation of collective bonds and poor coordination of atoms, transforming nanocrystallites to nanofluids.

Structural excitation during premelting and the coherent transformation from crystal to liquid, with coexistence of phases at photomelting, differ from the recrystallization process in which ‘hot forms’ of the lattice and the liquid phase coexist as a consequence of thermal contacts. The extent of structural changes and thermodynamics of melting are dependent on the size of nanoparticles.

The applicability of UEC and UEnC for the study of the structural dynamics on the surfaces, the study of the influence of the adsorbed molecules, the observation of the transitions from the crystal to the liquid phases [1-5] and the investigation of the surfaces with a variety of adsorbed molecules, molecular assemblies, different nanoparticles has been experimentally demonstrated. Here femtosecond laser pulses cause the coherent restructuring of the surface layers with sub-angstrom displacement of the atoms and non-equilibrium dynamics of the surface structure is determined from Bragg diffraction spots and rings.

In order to understand the underlying processes of the phase changes of the nanomaterials and different chemical reactions with their participation, it is required not only the structural imaging of the samples and their interfaces in steady conditions, but also the insight into their dynamics and the redistributions of their structure in real time. The development of ultrafast electron diffraction [3,6-12], ultrafast crystallography (UEC) [1,4], ultrafast electron microscopy [13, 14] and the dynamic transmission electron microscopy (DTEM) [15] allows combine atomic spatial resolution, achieved in the electron diffraction techniques, with high time resolution of the femtosecond laser experiments. In this context, the "optical pumping – electron diffraction probing" has led to an extremely powerful tool for the investigation of the structural dynamic processes in different materials.

The possibilities of application of the method, to not only the study of structural changes, but also the redistribution of the charge and energy at the interphase boundaries were shown [1, 4]. The UEnC method currently allows us to study such low surface densities of ~6 particles/μm^2, in fact, demonstrating the possibility of studying an isolated nanoparticle [1, 4]. Upon reaching the submicron dimensions of the diagnostic electron bunch, we should expect fundamentally new results of the study of 4D dynamics of nanostructures with a combination of diffraction and spectroscopic methods with ultrahigh temporal resolution.

1. TIME-RESOLVED ELECTRON NANOCRYSTALLOGRAPHY

This article shows the development of UEnC, a specific implementation of UEC, optimized for high sensitivity and high data acquisition efficiency and trained on the quantitative studies of different solid nanostructures with high temporal resolution ranging from nanoseconds to femtoseconds. Nanostructures are characterized by a number of unusual properties compared to their bulk counterparts. First of all, this is due to the manifestation of the quantum-size effect and the corresponding relatively-large percentage of structural units of the nanoparticle being on its surface. One of the structural features is the emergence of the so-called nano-crystallographic structure types [18, 19], which have a tendency to form closed shells and are connected with the appearance of magic numbers in the size distribution [20-22].

The morphology and lattice parameters of nanocrystals are strongly dependent on the substrate and the surface modification [23], which results in the contraction [24] and the formation of twin boundaries [25] due to the relaxation of the surface deformations.

Along with these new structural forms new properties appear, that is connected with the increased correlation between the electron degrees of freedom of the atomic structure on the nanometer scale. The capabilities for building nanostructures with specific properties via nano-synthesis, or self-assembly open rather interesting prospects of the use of the nanoparticles as building blocks for new devices with high specificity, speed and density which can be used in a variety of fields, such as electronics [26], photonics [27], magnetism [28], catalysis [29,30] and sensors [31].

The temporal resolution in UEnC greatly drops as compared to time-resolved electron diffraction of free molecules due to large paths of the electron bunch in the surface layer. At present the perspectives of the study of the dynamics in complex nanostructures with subpicosecond resolution appeared. For this purpose it is reasonable to implement the set of modern improvements such as the miniaturization in order to ensure the distances of the electron paths as short as possible [32], high accelerating field [33] for the generation of femtosecond electron bunches, RF-compression [34,35] to achieve the high brightness of the electron source, the photo-assisted field emission [36] for potentially high spatial coherence and the special compression scheme of the wave front to reduce the mismatch of light and electron velocities.

All these advances have opened new possibilities for investigation of the coherent structural dynamics of different nanomaterials with subpicosecond (femtosecond) temporal resolution.

1.1. BASIC CONCEPTS

The progress towards getting of quantitative information about the structural dynamics in the condensed state is still limited due to the difficulties in the understandings of the systematic effects in the diffraction patterns, obtained with a high temporal resolution, and due to the lack of the reliable schemes allowing solve the inverse problem of 3D atomic structure determination. The modern approach to the development of UEnC is aimed to the development of the robust methods of the data analysis and to the increase of the quality of the experiments [4]. In this field the starting point for initial experiments may be "powder diffraction", when the nanostructures are dispersed on the surface of the substrate with very low coating density as shown in Fig. 1 (a, b).

In Time-Resolved Electron Microscopy (TEM) when studying of a nanomaterial, placed on a mesh, possible defects in the film may introduce artifacts in the diffraction data. Furthermore, intense laser radiation may cause fracture of the mesh. To avoid these

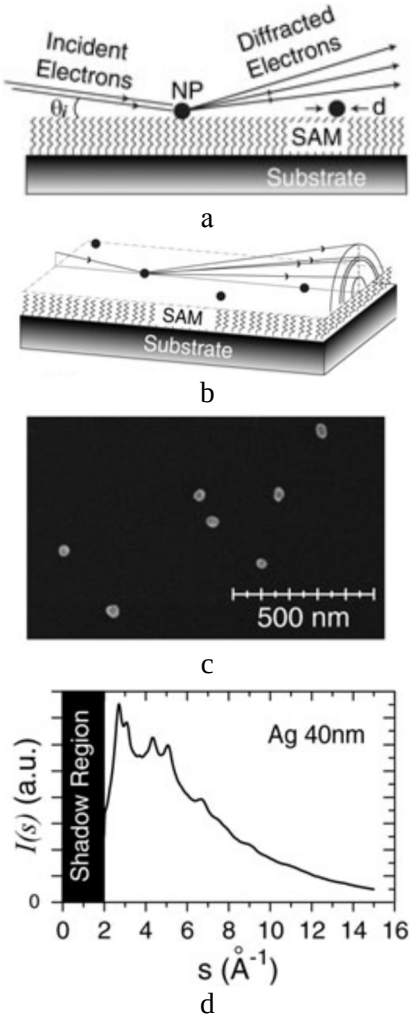

Fig. 1. Nanopowder on the surface of the substrate. a, b: The electron beam diffraction in the solid angle of 0-2π at sliding reflection from the substarte surface with the nanoparticles. The angle of incidence is 1-5°. In order to minimize the interference caused by the electron scattering from the substrate the "soft" buffer layer is used lifting the nanoparticles above the substrate and thus suppressing this background signal. c: Ag nanoparticles with average size d of ~ 40 nm dispersed on the Si(111)-surface are observed by scanning electron microscopy (SEM). d: The intensity of scattering I(s) for Ag nanoparticles [4]

Рис. 1. Нанопорошок на поверхности субстрата. a, b: Дифракция электронного пучка в телесном угле 0-2π при скользящем отражении от поверхности подложки, на которую нанесены наночастицы. Угол падения составляет 1-5°. Чтобы минимизировать интерференцию, вызванную рассеянием электронов от подложки, используется «мягкий» буферный слой, поднимающий наночастицы над подложкой и тем самым подавляющий этот фоновый сигнал. c: наночастицы Ag, имеющие срадний диаметр d ~ 40 нм, диспергированные на поверхности Si (111); наблюдение с помощью сканирующей электронной микроскопии (SEM). d: интенсивность рассеяния I (s) для наночастиц Ag [4]

parasitical effects and in order to perform more comprehensive investigations which include the study of the dynamics of the interface, the particles are usually placed at the surface of a solid substrate. A sliding elec-

tron beam is being used to probe these particles. In addition, a self-assembled monolayer (SAM) of aminosilane is being used as a buffer layer. Aminosilane molecules have three important functions [37]:

(1) It helps to suppress the diffraction signal caused by the substrate, which (in the absence of aminosilane) gives strong background signal greatly exceeding the diffraction signal from the nanoparticles.

(2) Allows obtain the diffraction pattern in 2π–solid-angle.

(3) Provides the control of the charge of the nanoparticles and the rate of heat transfer.

In order to minimize the probability of subsequent electron scattering on the second particle, it is required to maintain the optimum density of nanoparticles:

$$\rho_{opt} = \sin^2\left(\theta_i / d^2\right), \quad (1)$$

where θ_i – the electron beam incidence angle and d is the diameter of the nanoparticles. Fig. 1 (c) shows SEM image of typical sample that meets these criteria. The mentioned Ag nanoparticles are 40 nm in diameter. These nanoparticles were scattered on the SAM layer applied to the Si(111)-substrate with the density of ~1 μm^{-2}. The data were acquired during ~1 min (Fig. 1-d). Note, that the diffraction pattern has fairly good signal/noise ratio, despite the fact that the nanoparticles occupy only 1% of the scattering region. This result is very different from data produced by similar experiments utilizing X-rays or neutron scattering, where high bulk density of the sample and large size of the particles are required (from microns to mm) due to the relatively low scattering cross-section (~10^{-4} to 10^{-5} times less than the scattering cross-section for the electrons).

1.2. SAMPLE PREPARATION

In order to obtain the diffraction patterns which would allow for quantitative interpretation of the experimental data it is required to prepare the surface of the substrate. The rather important prerequisite in this procedure is adequate molecular buffering of the substrate surface, allowing one to control the dispersion of the nanoparticles and to suppress of the extraneous electron scattering from the substrate. The sample preparation for UEnC is rather similar to the techniques developed in molecular electronics [31, 38, 39], which provide rather useful approaches for the building of "SAM – nanoparticle" interfaces. Five major steps of this process are shown in Fig. 2.

(a) Si substrate is functionalized by hydroxyl groups using a modified RCA procedure [40]. The hydroxyl layer thickness is 1-5 nm.

(b) Functionalized Si substrate is then immersed for 20 min in a solution of surface active compounds, containing terminal amino groups (-NH_2) and polar group (-$Si(OMe)_3$). SAM layer is being formed on Si surface via silanization process. $Si(OMe)_3$ groups react with the hydroxyl groups on Si surface, forming SAM layer coating with aminogroups, located on the outer side of the layer.

(c) Formation of more compact and organized SAM layer is performed by lipophilic interactions between alkanes, which usually takes a few hours. Note, that this process takes place at a certain temperature. The sample is placed in an oven and heated to 80 ºC at the atmosphere of dry nitrogen of high purity [38].

(d) Terminal amino groups are protonated by placing the sample in a weak acidic solution. The protonated aminogroups are required for subsequent binding of the negatively-charged colloidal particles of Au clusters [31, 41, 42].

(e) The sample is removed from the solution and dried in a nitrogen atmosphere.

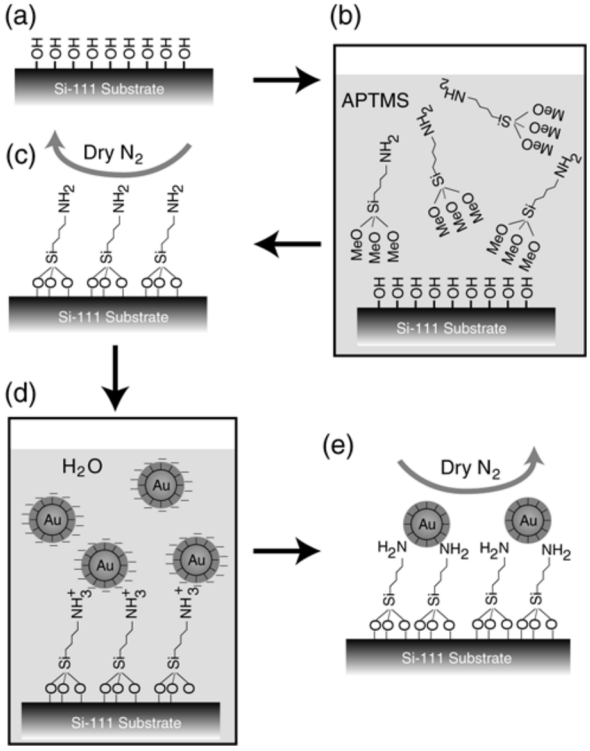

Fig. 2. Schematic diagram of the sample preparation. The steps include **a**: cleaning the surface of Si using a modified RCA procedure; **b**, **c**: dispersing the nanoparticles [4]. **d**: terminal amino groups are protonated by placing the sample in a weak acidic solution. The protonated aminogroups are required for subsequent binding of the negatively-charged colloidal particles of Au clusters. **e**: the sample is removed from the solution and dried in a nitrogen atmosphere [4]

Рис. 2. Принципиальная схема пробоподготовки образца. Этапы включают: **a**: очистку поверхности Si с использованием модифицированной процедуры RCA; **b**, **c**: диспергирование наночастиц [4]; **d**: протонирование терминальных аминогрупп путем обработки образца раствором слабой кислоты. Протонированные аминогруппы необходимы для последующего связывания отрицательно заряженных коллоидных частиц кластеров Au. **e**: удаление образца из раствора и высушивание его в атмосфере азота [4]

Controlled dispersion of nanoparticles is achieved by choosing the acidity and hydrophobicity of the solution. The density of binding -NH_2 groups may be controlled by adding a weak acid (e.g. Acetic) [43], which determines the final optimal dispersion of the nanoparticles. Fairly accurate control of their dispersion on the surface can also be achieved via hydrophobicity of the solution. Remember, that terminal amino groups are hydrophilic. By adding a suitable amount of ethanol, the overall hydrophobicity of the solution can be controlled [44]. The effect of acidity change is shown in Fig. 3 (a, b).

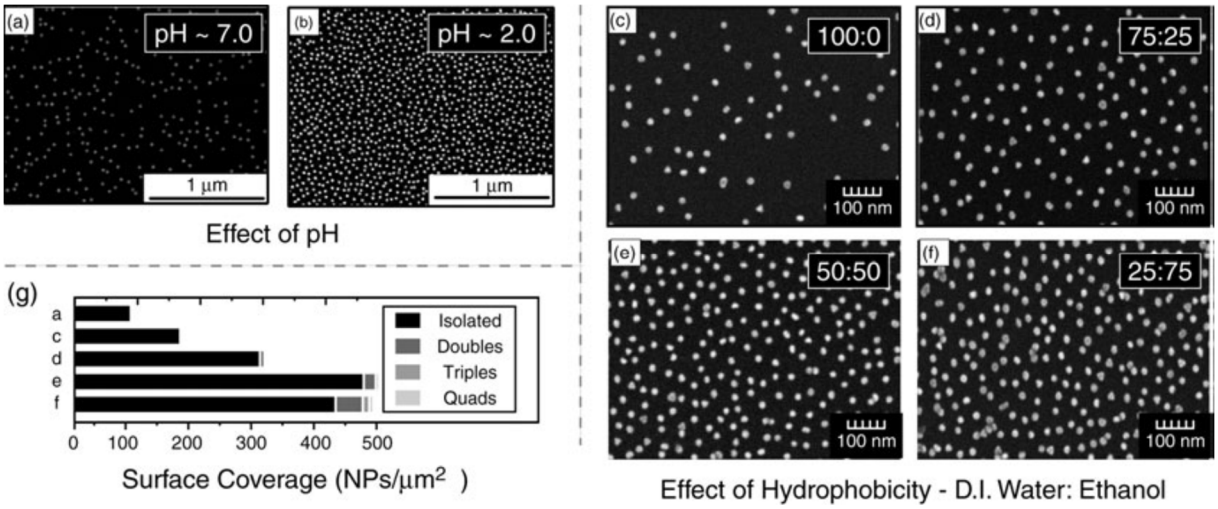

Fig. 3. SEM images, showing the controlled deposition of gold nanoparticles on the surface of Si (111), which is achieved by controlling of pH of the sol of gold nanoparticles and hydrophobicity of functionalized Si(111)-surface. By adding a suitable amount of ethanol, the overall hydrophobicity of the solution can be controlled. a, b: The effect of acidity change is shown. c – f: illustrates the distribution of the nanoparticles for four different concentrations in the mixture of ethanol and deionized water. Note, that the density of the coating changes from 160 μm^{-2} to 508 μm^{-2} with the increase of ethanol concentration. The histogram g shows the increase in particle agglomeration when the degree of surface coating is increased [4]

Рис. 3. СЭМ - изображения, показывающие контролируемое осаждение наночастиц золота на поверхности Si(111), что достигается путем регулирования pH золя наночастиц золота и гидрофобности функционализированной поверхности Si(111). Добавляя подходящее количество этанола, можно контролировать общую гидрофобность раствора. a, b: показан эффект изменения кислотности. c - f: иллюстрирует распределение наночастиц для четырех различных концентраций в смеси этанола и деионизированной воды. Следует отметить, что плотность покрытия изменяется от 160 до 508 мкм$^{-2}$ с увеличением концентрации этанола. Гистограмма g показывает увеличение агломерации частиц при увеличении степени поверхностного покрытия [4]

By adding acetic acid to the solution, it is possible to dramatically change the coating density of the nanoparticles from 70 μm^{-2} at pH = 7 to 300 μm^{-2} at pH ~ 2. The increase of the concentration of ethanol decreases the hydrophobicity of the solution, which correspondingly increases the mobility of the nanoparticles and leads to the noticeable change in their distribution. Fig. 3 (c-f) illustrates the distribution of the nanoparticles for four different concentrations in the mixture of ethanol and deionized water. Note, that the density of the coating changes from 160 μm^{-2} to 508 μm^{-2} with the increase of ethanol concentration.

1.3. THE INITIAL DATA ANALYSIS

This section describes the initial processing of the “powder diffraction” patterns according to the work [4]. Just as in the method of the “common” diffraction with continuous electron beam, or TRED (please, see Part I and II of this article), this procedure is required step in UEnC, which allows obtain the scattering function *S(s)* and its Fourier – transformation, the radial distribution function of the inter-nuclear distances, *G*(*r*). Here the electron momentum transfer ***s*** is determined by the standard equation:

$$s = |k_0 - k_s| = \frac{4\pi}{\lambda}\sin(\theta/2), \qquad (2)$$

where ***k*** – the wave vector, $k = |k| = \frac{4\pi}{\lambda}$, $\boldsymbol{k}_0$ and $\boldsymbol{k}_s$ – the wave vectors of the incident and the scattered electrons; λ – electron wavelength and θ is scattering angle. The details of initial data analysis depend on the experimental technique (the electron diffraction, X-rays, or neutrons). However, all of them consist of the determination of the total scattering intensity *I*(*s*), the component of *S*(*s*) function, along with the incoherent background from atomic scattering and subsequent normalization using the atomic scattering amplitudes. The Fourier transformation of the function *S*(*s*) gives

the radial distribution function of the interatomic distances $G(r)$. The validation of this approach can be performed by determining of $S(s)$ and $G(r)$ for the well-known structures. All necessary steps in the initial data processing are shown in Fig. 4.

The first step is to obtain the total scattering intensity $I_{tot}(s)$ by the radial averaging of Debye-Scherrer rings from the nanopowder. Here it is necessary to define the centers of these rings, which can be done by averaging of symmetrical diffraction curves for different angular sectors of the rings. Of course, it is important to consider the incidence angle of the electrons, the sample orientation, the distance from the scattering point and the vertical deviation of the primary beam in the image plane.

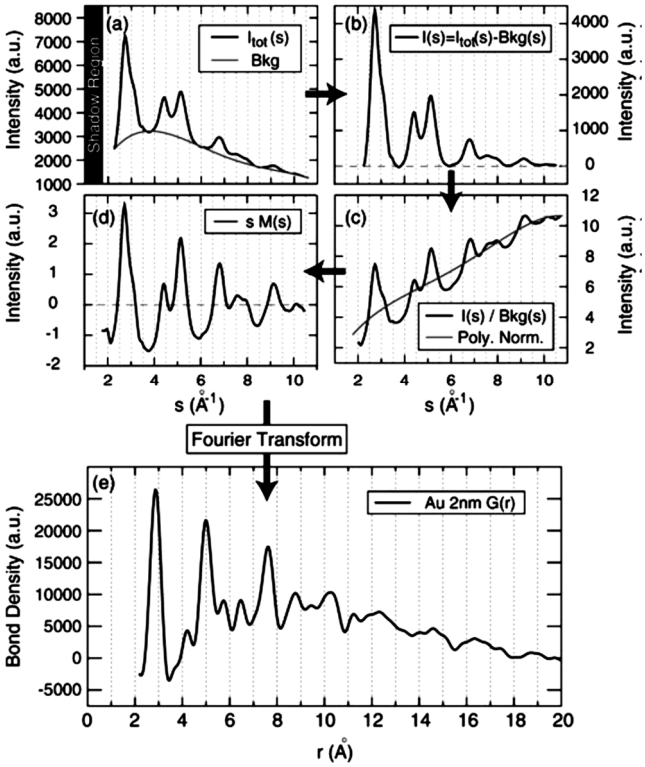

Fig. 4. Data of pre-processing steps in UEnC, which lead to obtaining *S(s)* function and the radial distribution of the inter-atomic distances *G(r)*, corresponding to the total scattering intensity $I_{tot}(s)$ [4]
Рис. 4. Шаги предварительной обработки данных в методе UEnC, которые приводят к получению *S(s)* - функции и функции радиального распределения межатомных расстояний *G(r)*, соответствующей полной интенсивности рассеяния $I_{tot}(s)$ [4]

When the center of the rings is found, $I_{tot}(s)$ is obtained and $I_M(s)$ is determined, then the function $R(r)$ can be calculated. The common relations between the functions $I(s)$ и $R(r)$ are given in the work [45]:

$$I_s(s) = I_A(s) + I_M(s) \quad (3)$$

$$I_A(s) = N\langle f\rangle^2 + I^{inelastic}(s) \quad (4)$$

$$I_M(s) = N\langle f\rangle^2 \int R(r)\frac{\sin(sr)}{sr}dr\,. \quad (5)$$

Here the incoherent background $I_A(s)$ consists of the atomic scattering and inelastic scattering $I^{inelastic}(s)$.

$$R(r) = 4\pi r^2\rho(r), \quad (6)$$

where $\rho(r)$ is the atomic density. Both functions are fairly smooth and can be approximated by a polynomial with appropriate order [46]. In Eqs. 3-5 f is atomic scattering factor, while N is the total number of the scattering atoms. It should be noted, that $I_s(s)$ and $I_M(s)$ greatly depend on the scattering geometry.

For example, in the experiments where the electron scattering occurs upon its reflection, the both components are changing compared with the traditional functions, used in the clearance scattering geometry, and it is important to introduce the so-called formative "absorption" function. Finally, the radial distribution of interatomic distances is calculated as following:

$$G(r) = \frac{2}{\pi}\int_0^\infty s[S(s)-1]\sin(sr)ds \quad (7)$$

$I_M(s)$ function for the ground state of 2-nm gold nanoparticles, obtained using above-mentioned processing procedure, is shown in Fig. 5, where it is compared with the calculated scattering intensity for the known cubic octahedral, decahedral and icosahedral structures.

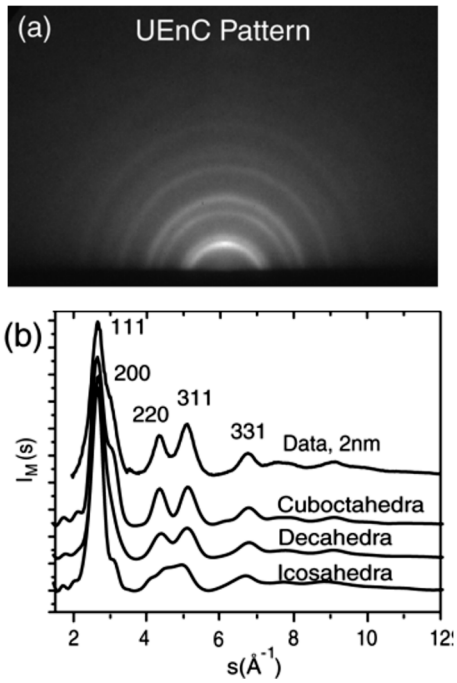

Fig. 5. The UenC diffraction pattern (a) and the experimental functions S(s) for 2-nm gold nanoparticles (b); also, the theoretical curves are presented calculated for octahedron, decahedron and icosahedron models of gold nanparticles[4,35]
Рис. 5. а: Дифракционная картина UEnC (a), экспериментальные функции S(s) для наночастиц золота (b), имеющих средний диаметр 2 нм; представлены также теоретические кривые, рассчитанные для октаэдрической, декаэдрической и икосаэдрической моделей наночастиц золота [4,35]

It is clearly seen, that the experimental data are in good agreement with the theoretical function for the perfect cuboctahedral structure, which is calculated based on the limited face-cenred cubic structure (fcc). The experimental and the calculated curves of $G(r)$ are shown in Fig. 6, where they are compared with the inter-atomic distances for fcc lattice. It can be seen, that within 0.05-Å accuracy the experimental data are in good agreement with fcc.

Remember, that $[S(s) - 1]$ is equivalent to the function $M(s)$, which is commonly used in the electron diffraction (see Part I), but "modified radial distribution function" $G(r)$, or $f(r)$, because $G(r) = 4\pi r\rho(r) = R(r)/r$, is a reduced form of the function $R(r)$. Therefore, $G(r)$, or $f(r)$ are the Fourier transforms of $sM(s)$:

$$G(r) = \frac{2}{\pi}\int_0^\infty sM(s)\sin(sr)ds \quad . \qquad (8)$$

For the experiments in the reflection geometry, the proposed procedure for the initial data analysis is not explicitly connected with $f(s)$ functions and is rather useful for UEnC data processing, because the incident electron angle is being optimized *in situ* depending on the interface configuration. The total scattering intensity and hence the value of N is determined via fitting of $I_A(s)$ to the canonical form $\langle f(s)\rangle^2$ in transmission electron diffraction for sufficiently large values of s, where the contribution of the inelastic component, $I^{inelastic}(s)$ and the absorption effects are negligible.

When analyzing the data for the excited electron states, in addition to the change of the diffraction pattern, caused by the structural dynamics, it is important to take into account also the "distortion effect", associated with Coulomb electron beam refraction, caused by a photo-induced surface potential. Since our probe is the charged-particles beam, the electrons can be deviated by photo-induced potential at the interface, caused by the photo-induced charge redistribution. This leads to the displacement of the diffraction pattern. By measuring the shift of Coulomb refraction, it is possible to determine the transient photo-potential associated with the charge transfer in the surface layer. Note, that non-uniform shift of the rocking curve in the reflection electron diffraction due to the charge transfer at the surface is discussed in the paper [47]. In the experiments with the powders, this shift is usually perpendicular to the surface and distorts the circular symmetry of the diffraction rings toward the edge of the shade of the central beam, which correspondingly causes the displacement of the central scattering angle ($s = 0$) from the direction of the original electron beam. This leads to a phase shift of $sM(s)$ and, correspondingly, of $G(r)$.

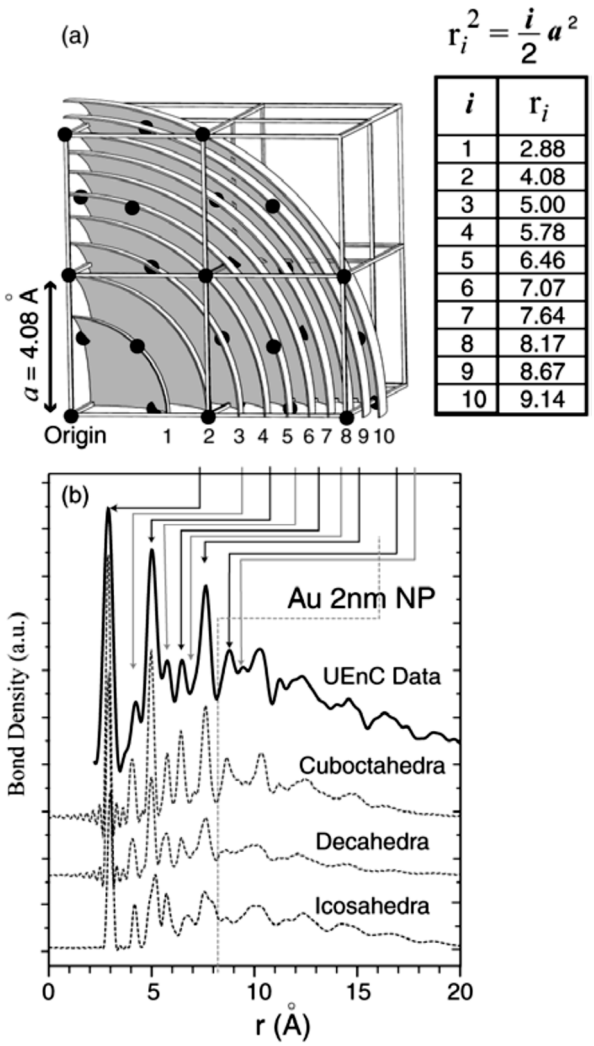

i	r_i
1	2.88
2	4.08
3	5.00
4	5.78
5	6.46
6	7.07
7	7.64
8	8.17
9	8.67
10	9.14

Fig. 6. The structural analysis of the 2 nm gold nanoparticles. **a**: the coordination of (fcc) shells corresponds to the inter-atomic distances r_i, calculated based on the bond order (i) and the known lattice constant a = 4.08 Å for Au. **b**: Experimental modified radial distribution functions for Au nanoparticles obtained in a static diffraction mode and theoretical curves for cubic octahedron, decaoctahedron and icosahedron [4,35]

Рис. 6. Структурный анализ наночастиц золота (средний диаметр 2 нм). **a**: Координация (fcc) оболочек соответствует межатомным расстояниям r_i, рассчитанным на основе порядка связи (i) и известной постоянной решетки a = 4,08 Å для Au. **b**: Экспериментальные модифицированные функции радиального распределения для наночастиц Au, полученные при дифракции непрерывного пучка электронов и теоретические кривые для кубооктаэдра, декаоктаэдра и икосаэдра [4, 35]

However, the phase shift is present implicitly in the complex transformation of $G(r)$ extraction, which is based on the total amplitude. This idea can be used to implement an iterative scheme of "Fourier-phasing" process, which re-symmetrizes the diffraction pattern with the angular dependence of the Coulomb refraction. It has rather simple form in the case of the dipole Coulomb field (Fig. 7):

$$V_s / V_0 = [(\theta_0\delta - \theta_i\theta_0 + \delta^2/2)^2 - \theta_i^2(\theta_0 + \delta)^2] / (\theta_i + \theta_0)^2, \quad (9)$$

where V_s – is adjustable parameter that is used to generate the observed shift $\delta = (\theta'_0 - \theta_0)$ of the Bragg peaks and V_0 is the initial electron energy.

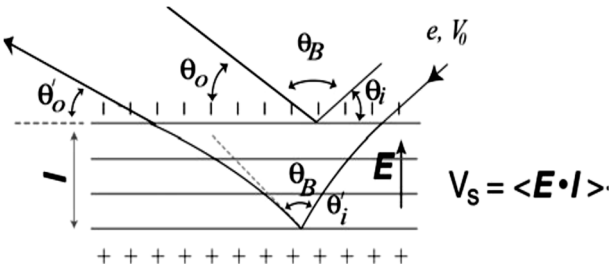

Fig. 7. Photo-induced Coulomb refraction of the diffraction pattern. Here θ_i – incidence angle of the electrons, $(\pi-\theta_B)$ - Bragg scattering angle, θ_0 – the angle of the electron exit in the absence of the photo-induced field E; θ'_i - the incidence angle of electrons and θ'_0 is exit angle of the electrons in the presence of the photo-induced field E; l - the depth of the electron penetration [4]

Рис. 7. Фотоиндуцированная кулоновская рефракция дифракционной картины. Здесь θ_i - угол падения электронов, $(\pi - \theta_B)$ - угол брэгговского рассеяния, θ_0 - угол выхода электрона в отсутствие фотоиндуцированного поля E; θ'_i - угол падения электронов и θ'_0 - угол выхода электронов в присутствии фотоиндуцированного поля E; l - глубина проникновения электронов [4]

For complex fields which cannot be satisfactorily modeled by the dipole Coulomb potential, the angular dependence is determined by either by the tracing of the electron beam, or by in situ extracted from Coulomb refraction effect. In the latter case a low-degree polynomial is utilized for the representation of the angular dependence. Then parameters of the polynomial are recalculated for the correction of the distortion of the anisotropic Bragg diffraction pattern caused by the interfacial Coulomb forces. The iteration of the symmetry of the image and Fourier-phasing allow for simultaneous determination of both the surface potential and the structural changes from the diffraction patterns.

Here *the temporal resolution* is determined by the effective width of the electron pulse and usually it is in the range from 200 fs to several picoseconds, depending on the incidence angle and the size of the electron bunch. The sequence of the electron pulses is programmed in such a way that they arrive either before the excitation of the sample (at negative times) or after the pump laser pulse (at positive times) with the temporal intervals corresponding to the rate of the structural changes.

To study the structural dynamics of the nanoparticles, the changes of the diffraction patterns should be traced up to a few nanoseconds [1, 4]. It allows monitor the long-term process of diffusion relaxation (compared to the structural dynamics of the photo-excitation, which takes place on the femto-picosecond time scales). In order to observe the subsequent recovery of the ground state and its reproducibility, it is required to acquire the diffraction patterns in the temporal intervals of up to 1 ms. For each time delay the acquisition time is ~20-100 s at the pulse repetition rate of 1 kHz. Here the diffraction pattern is usually recorded for ***s*** values in the range of 1-15 $Å^{-1}$. From the obtained diffraction patterns it is possible extract *in situ* the transient structure, its temperature and the charge of the nanoparticles, as will be shown in the next section.

2. EXPERIMENTAL RESULTS

2.1. MELTING OF AL UNDER STRONGLY DRIVEN CONDITIONS

The first grainy pictures with sufficient diffraction orders to resolve atomic motions involved in a structural transition on the prerequisite subpicosecond (10^{-12} s) time scale were recorded by Miller et al. [32] and are shown in Fig. 8A. These frames catch the simplest possible structural transition – the act of melting – but under rather special boundary conditions involved with strongly driven phase transitions [48]. The particular question being addressed by this work dates back to a long-standing debate in the 1930s concerning the onset of the liquid state [49]. This issue also has ramifications for understanding the state of matter in other extreme conditions, such as the interior of planets or stars [50]. To put this question in proper context, consider the melting of a block of ice. We all know ice melts from the surface. We also know that if we direct a blow torch to the ice it will melt faster. This everyday experience is referred to as heterogeneous nucleation. What if you could heat up a material so fast that based on extrapolations of heating rates and melt velocities, you would predict that the material should melt faster than the atoms could move or, more correctly, faster than the speed of sound? The answer can be gleaned from this data (Fig. 8A) directly, without a high level of analysis [12,51]. The experiment used a special "blow torch" – In this case, a femtosecond laser system – to achieve heating rates approaching 10^{15} K/s for Al (as opposed to ice in the above analogy). At 500 fs, you can see high-order diffraction rings illustrating that the Al is still in its nascent face-centered cubic (FCC) lattice. At 1.5 ps, you can see these rings become dimmer as the initially photoexcited electrons lose energy to lattice phonons. The increase in root mean square (RMS) motion of the atoms reduces the lattice coherence and corresponding diffraction as described by temperature-dependent Debye-Waller factors. The most astonishing event happens between 2.5 ps and 3.5 ps. There is an incredibly fast lattice collapse in which bonds are broken and the first coordination number of

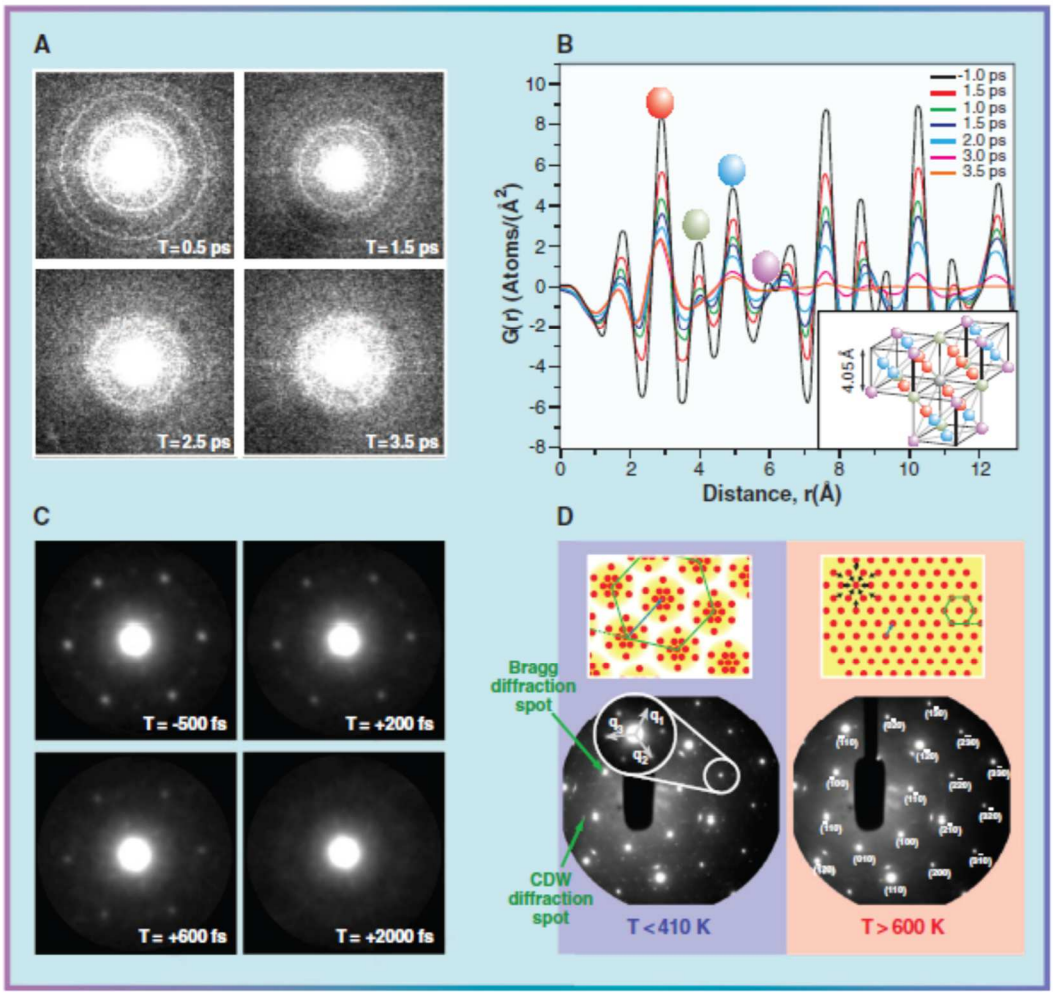

Fig. 8. Evolution in femtosecond electron diffraction. A: The first grainy frames of an atomic movie of the photo-induced melting of Al in intensive field of laser radiation. It is possible to see by eye the increased thermal motion leading bond breaking (0.5 to 2.5 ps) and collapse of the FCC lattice to the shell-like structure of a liquid (2.5 and 3.5 ps). B: The transformation of diffraction intensity in a space of internuclear distances [32]. C: The dramatic improvement in femtosecond electron diffraction, in which it is possible to directly observe (reciprocal space) the atomic motions involved in the suppression of charge density waves (CDWs) in $TaSe_2$ for a single diffraction order out of hundreds to give the structural changes. An expanded view of the two different structures as observed in electron diffraction is shown with a schematic representation of the atomic motions captured on the 100-fs time scale [52]. B, C: $TaSe_2$, in which one observes similar effects – however, with important differences owing to different inter-plane couplings. (From ref. [48])

Рис. 8. Эволюция фемтосекундной дифракции электронов. A: Первые кадры атомного фильма фотоиндуцированного плавления Al в интенсивном поле лазерного излучения. На глаз можно наблюдать усиление теплового движения атомов, ведущее к разрыву связей (от 0,5 до 2,5 пс) и коллапс FCC решетки до оболочечной структуры жидкости (2,5 и 3,5 пс). B: Преобразование дифракционной интенсивности в пространство межъядерных расстояний [32]. C: Резкое улучшение фемтосекундной дифракции электронов, в котором можно непосредственно наблюдать (обратное пространство) атомные движения, участвующие в подавлении волн плотности заряда (CDWs) в TaSe2, для одного порядка дифракции из сотен, приводящих к структурным изменениям. Показано увеличенное изображение двух различных структур, наблюдаемых при дифракции электронов, и схематическое представление атомных движений, полученное в масштабе времени 100 фс [52]. B, C: В $TaSe_2$ наблюдаются аналогичные эффекты, однако с важными различиями вследствие различий в межплоскостных взаимодействиях [48]

the FCC lattice goes from 12 to an ensemble average of 10 for the unstructured shell-like structure of a liquid [48]. Once reaching the critical point for this degree of superheating, the whole melting process occurred within 1 ps. This time scale has to be fully appreciated. This is 10 times faster than this process could occur through normal heterogeneous nucleation. Rather than melting from the surface in an “outside-in” fashion (heterogeneous nucleation), the system was melting from the “inside out” (homogeneous nucleation). This provided an atomic view of homogeneous nucleation that could be used to test the accuracy of atomistic molecular dynamics calculations [53]. From the real space transform, it was possible to discern that the largest changes involve shear atomic motions, with the collapse of the transverse barrier as part of forming the

liquid state. These observations showed how to control nucleation growth to as few as 10 atoms and avoid cavitation-induced shock waves and thermal damage in laser-driven ablation [48]. On the basis of this new insight, a picosecond infrared laser tuned to the OH stretch of water in tissue was developed for laser surgery, with the correct temporal profile to restrict nucleation growth. This method has now been shown to be capable of cutting tissue without scar tissue formation [54]. Subsequent work in the area has primarily focused on photoinduced phase transitions. On the femtosecond time scale of the photoexcitation process, the lattice is effectively frozen. The optical transition to a higher lying electronic state instantaneously changes the electron distribution relative to the time scale of nuclearmotions. This provides an opportunity to observe the effects of changes in electron distribution and electron correlation energies on bonding by observing the atomic motions in response to these changes [12, 51]. These studies include strongly driven phase transitions involved in nonthermal melting or electronically driven nucleation effects [55, 56]; creating states of warm dense matter with a counterintuitive apparent increase in bond strengths at high excitation levels [50]; and the observation of highly cooperative, coherent, responses to weak perturbations of strongly correlated electron-lattice systems [57]. With respect to the latter case, the highest-quality atomic movies of structural transitions have been observed in layered compounds that exhibit interesting two-dimensional effects on electron correlation energies and bonding [12, 48, 51, 57].

Charge density waves (CDWs) are examples in which a small modulation of the atomic positions in the plane leads collectively to higher overall lattice stability [48]. By photoinducing a change in charge distribution, this delicate balance in forces between intra- and inter-plane coupling is modified, and the lattice relaxes to a higher symmetry state. The atomic movie of the photoinduced suppression of the CDW modulation in TaS_2 is particularly interesting; one can observe a dramatic effect in which both the suppression and reformation of the CDW occur at the fundamentally fastest possible speeds [48]. This work has been extended to other related systems [52, 58], such as $TaSe_2$ (Fig. 8, B and C), in which one observes similar effects – however, with important differences owing to different inter-plane couplings. When one observes such a collective effect at the atomic level, there is an immediate appreciation of the highly cooperative nature of strongly correlated electron-lattice systems. The visual connection to the many-body effects helps to drive home the operating physics in a single measurement. Effectively, it is a direct observation of the electron-lattice coupling [48].

From a chemistry perspective, the real power of high–bunch charge and -brightness electron sources has been recently demonstrated by using femtosecond crystallography to follow the photo-induced reaction dynamics of organic systems [48, 59, 60], the mainstay of chemistry. This class of materials invariably as low thermal conductivities and involve large-amplitude motions as part of the reaction dynamics that greatly limit the sampling rate and number of photocycles. In addition, organic systems have much more complex structures than do the solid-state systems discussed above. There were hundreds of diffraction orders that went out to better than 0.4 Å to serve as constraints in the determination of the time-dependent structures. The signal-to-noise ratio of a single diffraction order is comparable with high quality, integrated, all-optical pump-probe measurements, but with direct connection to structure [59].

2.2. PHOTOINDUCED STRUCTURAL CHANGES IN GOLD NANOCRYSTALS

The *unexpected* discovery of non-crystallographic structural types of different nanoclusters [20, 25] and their variations [its form fluctuations [61], the pre-melting [23, 62], the structural variety of different gold and silver clusters and their experimentally-observed inter-conversions prompted a large number of the researchers to their intensive study in the last two decades. The investigations of gold clusters, passivated by alkylthiolates, showed that the size of the clusters was changing discretely and had rather unusual stability.

The possibility for direct observation of the structural change was first demonstrated by high-resolution transmission electron microscopy. In those experiments, continuous electron beam was utilized for the sample heating [63]. Probably the most interesting phenomenon is "surface pre-melting", when at the early stage of the process the formation of a liquid surface layer on the core of the particles takes place, which results in the subsequent melting. This mechanism has been invoked to explain the changes in the shape of the gold nanorods [64], the premature decrease in the intensity of the reflection [65], the saturation of acoustic frequency [66] and the coalescing of the gold nanoparticles after its photo-excitation by the laser pulses at temperatures below the melting point [67].

The experimentally-observed non-uniform dynamics of the atoms during the Au-surface melting is consistent with the theoretical concepts proposed in the papers [62, 68]. Ruan and co-workers studied the structural dynamics of 2-nm gold nanoparticles photo-ex-

cited by 800-nm laser pulses [37]. Such photoexcitation allows avoid the plasmon resonance and subsequent photomechanical sample modification [69].

Using the difference diffraction patterns, the structural changes after the pulsed laser heating of the nanoparticles were determined (Fig. 9). Such investigations were done:

(a) in the reciprocal space in order to establish the loss of the long-range order based on the Bragg peak analysis.

(b) in the real space to determine the changes of the short-range order based on the analysis of density of the inter-nuclear distance function $G(r)$.

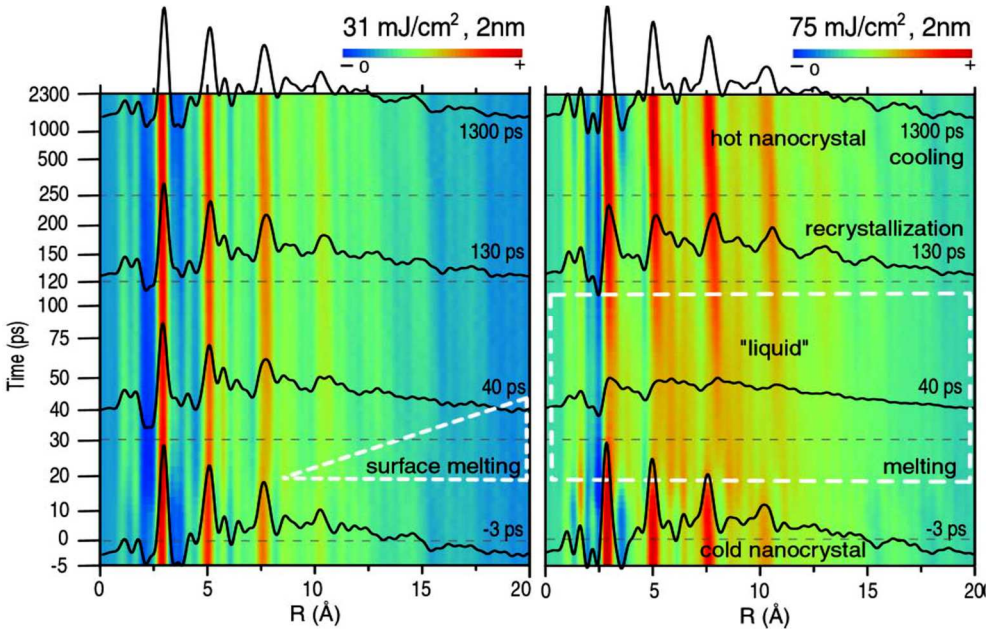

Fig. 9. The melting dynamics of 2 nm Au nanoparticles. Left: mRDF map constructed by stacking modified Radial Distribution Functions (mRDFs) of UEnC patterns at a sequence of delays between 5-2300 ps at irradiation fluence F=31 mJ/cm^2. Surface melting (enclosed by the dashed white line) is visible. Right: mRDF map for F=75 mJ/cm^2. Full scale melting is observed. The liquid state (enclosed by dashed white line) is characterized by the drop of 2nd nearest density (at ~ 5Å) to (1-1/e) of the static value (at negative time) [35]

Рис. 9. Динамика плавления наночастиц золота, имеюших средний размер 2 нм. Слева: модифицированные функции радиального распределения (mRDF) образцов, полученные методом UEnC при последовательных задержках во времени от 5-2300 пс и плотности энергии лазерного излучения F = 31 мДж / см^2. Видно плавление поверхности (штриховые линии белого цвета). Справа: mRDF для F = 75 мДж / см^2. Наблюдается полномасштабное плавление. Жидкое состояние (штриховая линия белого цвета) характеризуется падением второй ближайшей плотности (при ~ 5Å) до (1-1/e) от статического значения (отрицательное время, холодный нанокристаллит) [35]

The effective surface potential Vs (Eq. 9) is simultaneously clarified in the Fourier – phasing method. As shown in Fig. 9 (a), the "melting" occurs in three stages:

(1) 0-20 ps: the intensity of the Bragg peaks is reduced, which is presumably caused by the loss of medium-range order for 2-nm gold nanocrystals;

(2) 20-200 ps: the behavior of the Bragg peaks may be related with the coexistence of the disordered domains and with the partial recovery of the medium-range order;

(3) at 335 ps and after: the negative peaks largely disappear, while some of the weak positive peaks corresponding to the ground state of Bragg's spectrum of nanoparticles become stronger. This indicates an appearance of the transient state at an elevated temperature.

The loss of the middle-range order in the temporal interval of 0-20 ps can be explained by either the thermal disorder, or by a decrease of persistent length caused by partial melting. Thermal disorder is often taken into account in the Debye-Waller analysis, based on the concept of random, uniform distance variations over the entire crystal. The drop in Bragg's diffraction intensity is caused by an increase in the rms amplitudes of the atomic oscillations in the plane perpendicular to the corresponding Bragg plane and is defined by:

$$I(s, t > 0)/I(s, t < 0) = \langle u(t)^2 \rangle s^2/4, \qquad (10)$$

where u(t) is the amplitude of perpendicular oscillations. Assuming that the atomic oscillations are isotropic relative to their equilibrium positions, it is possible to determine the average oscillation amplitudes and then the temperature of the crystal from the loss of Bragg peak intensity. Ruan with colleagues [4] analyzed the time-dependent mean-squared amplitudes of

the oscillations in the groups (220), (311) and (331) of Bragg peaks and established the existence of the anisotropy between these three groups (Fig. 10). Here different Bragg peaks are consistent with the different values of the rms amplitudes, that cannot be explained within the model of homogeneous thermal fluctuations. The fact, that the high-order peak (331) corresponds to a lower degree of the ordering, comparing with the low-order peaks, suggests that the links of the large inter-atomic distances are subject to greater disturbance. Finally, it indicates a decrease of the persistence length for the nanocrystals.

To describe the local structures in this example we use the radial distribution function $G(r,t)$. As compared to the ground state, $G(r, t = -1\ ps)$, (Fig. 10b) in the range of 10-20 ps the correlation density, corresponding to the bonds of the nearest environment (~ 2.89-7.50 Å), falls in a substantially smaller proportion. This is a clear indication of the decrease in the lattice ordering and a significant decrease of the persistence length. When measuring the increase of the distances in the nearest environment, it is possible to get a preliminary estimation of the lattice temperature based on the thermal expansion coefficient [70]. It was determined experimentally, that the maximum temperature of the lattice (Fig. 10) is ~ 950 K [4], which is rather close to the value of 900 K, corresponding to the melting point under steady state conditions [71] for 2-nm gold nanocrystals, but is significantly higher that the temperature of the surface melting which is equal to 377 K [67].

Also it was studied the joint change of the potential V_s (Eq. 9) and the thermal expansion and it was shown that these processes take place at different time scales. Thus, by combining the analysis based on $sM(s, t)$ and $G(r, t)$ functions it is possible to relate the loss of long-range order and the decrease of the persistence length with the phenomenon of "non-homogeneous pre-melting." However, without quantitative 3D - modeling it is impossible to distinguish between "co-existence of phases", when the nanoparticles are divided into homogeneously-distributed crystallites and the disordered domains, and the "surface pre-melting", when a liquid layer forms a continuous surface, which thickness increases with the increase of the temperature [62, 72].

A reversible nonhomogeneous surface pre-melting of Au nanoparticles is demonstrated through molecular dynamics simulations [70]. With increasing temperature, liquid-like atoms first appear at some vertices and edges of surface facets, then small liquid regions grow and, at temperatures close to the particle melting temperature, most of the remaining solid-like surface atoms reside on {111} planes which are the most stable against surface premelting. The appearance of a contiguous liquid layer (complete surface premelting) is size dependent and is not observed in very small nanoparticles [70].

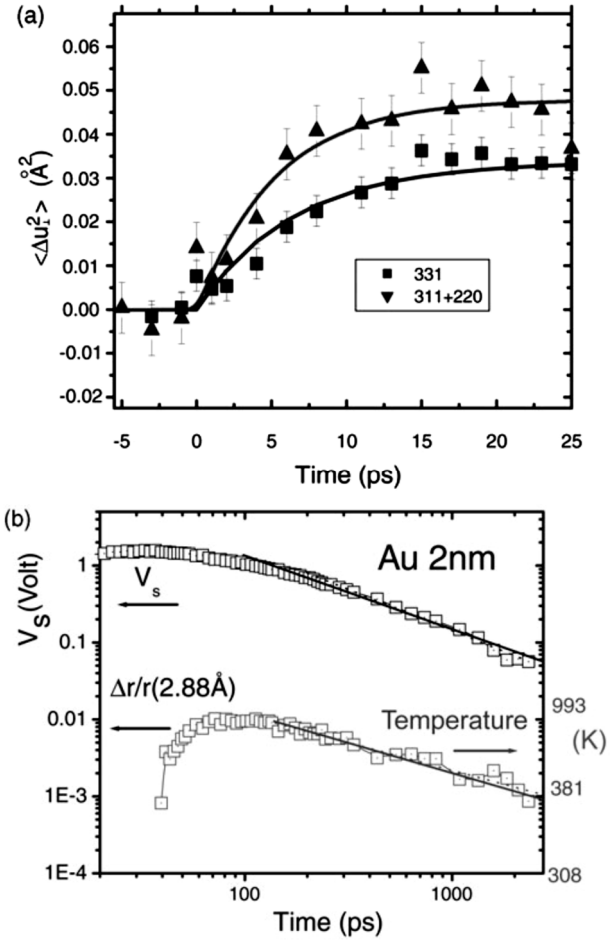

Fig. 10. a: The projections of the perpendicular amplitudes of atomic oscillations ‹Δu(t)^2›, derived from the intensity of Bragg peaks changes using Debye-Waller analysis. The anisotropy between the peaks is clearly seen, since the peak (331) corresponds to a lower degree of ordering than the peaks of lower order, indicating the reduction of the persistence length in the nanocrystals (see text). b: The transient surface potential V_s was measured in the nanoparticles (left axis). The lattice temperature was obtained by analyzing of the fluctuations of the nearest atoms while using the thermal expansion coefficient of the bulk material (right axis) [4]

Рис. 10. а: Проекции перпендикулярных амплитуд атомных колебаний ‹Δu(t)^2›, полученные из изменения интенсивности Брэгговских пиков; использован анализ методом Дебая-Уоллера. Ясно видна анизотропия между пиками, так как пик (331) соответствует более низкой степени упорядочения, чем пики более низкого порядка, что указывает на уменьшение длины персистентности в нанокристаллах (см. текст). В: Переходный потенциал поверхности V_s, измеренный в наночастицах (левая ось). Температура решетки получена путем анализа флуктуации ближайших атомов при использовании коэффициента теплового расширения объемного материала (правая ось) [4]

On the nanosecond time scale, is clearly seen the increase in the density of the correlation on slightly larger distances with respect to the structure of the ground state [70].

4D – refinement of the structure by the inverse Monte-Carlo method. The radial distribution function $G(r)$ is a one-dimensional (*1D*) projection of a 3D atomic structure containing only inter-atomic bonds of the first order. To calculate higher order bonds and to reconstruct a 3D atomic structure, it is required to propose a model structure and then refine its parameters using the experimental data. The nanostructures typically require more parameters comparing with the powders. To avoid ambiguity, when determining the structure, it is used the complex modeling method, which combines the theory and the experiment in a self-consistent procedure [73]. Fortunately, for small homo-nucleus Au crystals, the determination of the ground state is facilitated by the restrictions on symmetry of the crystal lattice with a resolution of ~ 0.05 Å. However, to determine the structure of the excited state, which has much lower ordering, the search process will diverge, since the number of possible solutions is increased and it is required to find the suitable parameters in order to restrict the space of their specification.

The solution of this 3D problem is based on the inverse Monte-Carlo method, which utilizes the modeling of the annealing to refine the structure and iterative scheme of the perturbations. It is known, that here the inverse Monte-Carlo method allows determine the global minimum. However, it may give ambiguous solutions. To resolve these ambiguities, it is required to utilize the algorithms, which allow introduce the constraints and direct the search of the global minimum [74]. In the work [4] it was proposed the refraining approach in the process of the search in the inverse Monte-Carlo method. The approach utilizes the reference points in UEnC data. These points are determined by the temporal interval between the neighboring diffraction patterns (frames), for which the structural changes between the neighboring conjugated time intervals are small. This provides a structural correlation between the frames and therefore allows tracking of the changes consistently and reliably in a limited search space, without requiring the global search. Using this approach, 3D transient structures of nanocrystalline gold were established.

Let's start with the model of the super-lattice of cuboctahedral 2.5-nm nanocrystal with the cubic cell size of 50 Å. The algorithm of the inverse Monte-Carlo method fits both $G(r)$ and $sM(s)$ functions to the experimental data in order to refine the structure of the super-lattice. In this approach, the sum of the squares of the differences of normalized experimental and theoretical $G(r)$ and $sM(s)$ functions, the functional χ^2, should be minimized. The results for selected temporal frames are shown in Fig. 11.

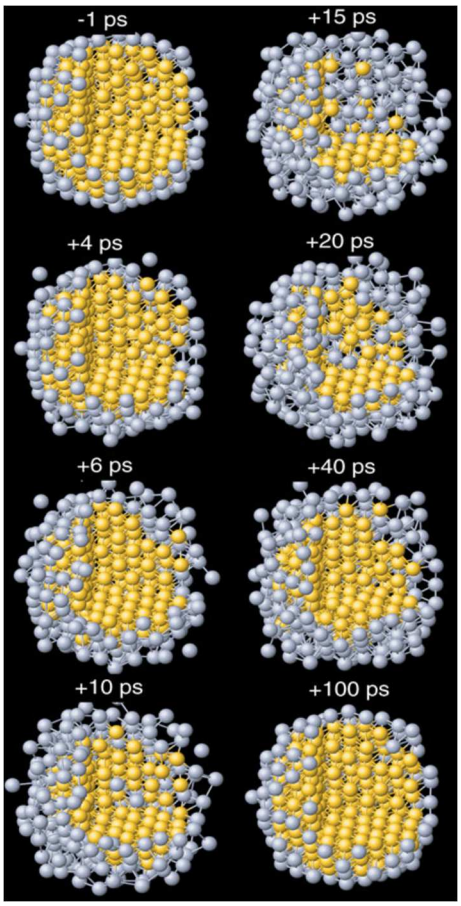

Fig. 11. The results of the use of the inverse Monte-Carlo method are given. The coordination of the Au atoms for different temporal delays shows that the melting process occurs via surface melting mechanism, but not via partial (bulk) melting [4]

Рис. 11. Результаты использования обратного метода Монте-Карло. Координация атомов Au для разных задержек во времени показывает, что в процессе плавления реализуется механизм плавления поверхности, а не механизм (объёмного) частичного плавления нанокристалла [4]

These 3D images show the features of the excited structures that are important for the choice of different scenarios of the melting process. It is clearly seen the emergence and development of the surface layer. With the increasing temperature, the surface layer becomes thicker, causing the compression of the crystal core. Note, that at the peak of the surface melting in the interval of 15-20 ps, less than 25% of the atoms are structured in the central core. Using the core size as a signpost, it is possible to trace the spread of the melting process and to observe the front of the solid phase. The proposed scheme for the refinement of 3D

structure helps not only to visualize the estimates based on the 1D difference diffraction analysis performed previously, but also offers the possibility for the determination of the correlated changes in the atomic structure of the higher orders. The last allow examine each step in the reorganization of the network of the local bonds during the phase transformation.

3. DIRECT OBSERVATION OF COHERENT OPTICAL PHONONS GENERATION IN NANOFILMS

The generation of coherent optical phonons in an antimony film has been directly observed by the femtosecond TRED method. The sample has been excited by a femtosecond laser pulse (λ = 800 nm) and probed with a pulsed photoelectron beam. Oscillations of the TRED intensity corresponding to vibration frequencies of optical phonons excited by the laser have been observed in the obtained diffraction patterns: totally symmetric (A_{1g}) and twofold degenerate (E_{2g}) phonon modes of antimony and their combinations [75].

Note that the coherent optical phonons arising under the impact of a high-power ultrashort laser pulse on a solid has been studied for a quite long time by optical spectroscopy and X-ray diffraction methods, particularly in semimetals, where the efficiency of their generation is relatively large (please, see, e.g., [76-79] and references therein). The drawback of optical methods is that the wavelength of the probing radiation (~1 μm) is much larger than the characteristic sizes at which the variations of the crystal lattice (~10 pm) occur. Therefore, they cannot determine the absolute value of atomic displacements, though, according to the results of the comparison of the data of optical and X-ray measurements performed in [76], they adequately demonstrate the dynamics of coherent vibrations of atoms in the crystal lattice.

In contrast to light, accelerated electrons (as well as X-rays) make it possible to obtain information about the dynamics of the distribution function of internuclear distances, which is the Fourier image of the diffraction intensity (please, see Part I), directly from the observed time-dependent diffraction pattern. The detection of the time behavior of the amplitude and shape of the diffraction maxima arising at electron probing makes it possible to determine the character of the motion of atoms within the unit cell under intense laser irradiation of the sample. Electron probing has another advantage because the scattering cross section of fast electrons is four or five orders of magnitude larger than the scattering cross section of X rays [5,80]. Therefore, electrons whose mean free path is many orders of magnitude less than that of X-ray photons can be used to probe thin samples, in particular, the optical-pulse-excited skin layer (~15 nm) of the antimony film studied in [75].

The space lattice of antimony refers to the rhombohedral system with two atoms in the cell A7 [20]. The structure of the complete representation of the vibrational modes of the structural type A7 has the form:

$$\Gamma = A_{1g} + A_{1u} + E_g + E_u, \qquad (11)$$

where A_{1g} and E_g are the optical modes active in the Raman spectra and A_{1u} and E_u are the acoustic modes. In the work [75], reported the first direct observation of the generation of *coherent optical* phonons in thin antimony films using the TRED method. To the best of our knowledge, only low-frequency *coherent acoustic* phonons in bismuth films were observed using this method in [81, 82]. The scheme of the experimental setup used in our experiments and implementing the TRED method is shown in Fig. 12.

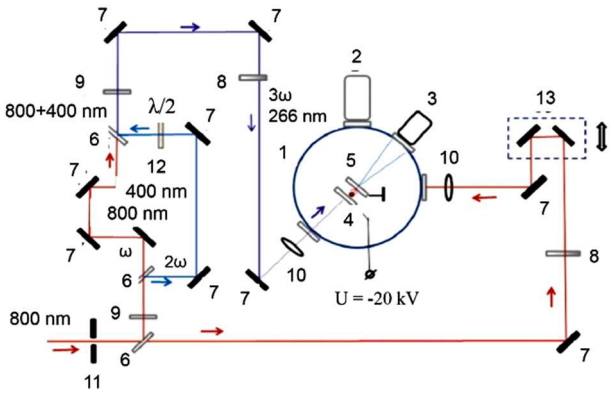

Fig. 12. Experimental scheme: (1) vacuum chamber, (2) turbomolecular pump, (3) amplifier of the electron current on the basis of microchannel plates and CCD chamber, (4) silver photocathode, (5) anode + target, (6) beam splitters, (7) mirrors, (8) radiation attenuator, (9) converters into the second and third harmonics, (10) lenses, (11) diaphragm, (12) polarization rotator, and (13) delay line [75]

Рис. 12. Схема экспериментальной установки: (1) вакуумная камера, (2) турбомолекулярный насос, (3) усилитель электронного тока на основе микроканальных пластин и CCD матрицы, (4) серебряный фотокатод, (5) анод + мишень, (6) делители лазерного излучения, (7) зеркала, (8) ослабитель излучения, (9) преобразователи лазерного излучения во II и III гармоники, (10) линзы, (11) диафрагмы, (12) вращатель плоскости поляризации лазерного излучения и (13) оптическая линия задержки [75]

The main frequency of a femtosecond Ti:sapphire laser (λ_1 = 800 nm) was used as the pump beam and the photoelectron beam formed under the irradiation of the semitransparent photocathode with the third harmonic of the Ti:sapphire laser (λ_2 = 266 nm) was used as the probe beam. In this manner, the optical and photoelectron pulses were strictly synchronized.

The laser pulse duration was 50 fs. The pulse repetition frequency was 1 kHz. The photocathode ma-

terial was a silver layer with a thickness of ~30 nm deposited on a thin quartz plate. The studied sample was an antimony film with a thickness of about 30 nm prepared by thermal deposition in vacuum on a standard carbon substrate with a thickness of 20–30 nm used in transmission electron microscopes. The pump laser radiation was incident on the sample at an angle of 45°. The energy density in the laser beam on the sample surface was 1.5 mJ/cm^2. Such radiation energy density made it possible to perform rather long-term measurements without noticeable degradation of the sample. The kinetic energy of probe photoelectrons was 20 keV.

The diameter of the electron beam in the region of the sample was ~0.1 mm. A lens based on a constant magnet adapted for the given energy of the electron beam served as a focusing system that made it possible to minimize the time-of-flight interval of electrons. The sample-diffracted electron beam amplified on the detector using microchannel plates got to the luminophore and was detected on a CCD camera.

Fig. 13 shows a typical electron diffraction pattern of the studied antimony film obtained in the absence of optical excitation. The presence of bright reflections unambiguously indicates the crystal (probably polycrystalline) nature of the studied sample.

The variation of the intensity of the diffraction pattern caused by the optical excitation of the sample was studied in the experiment as a function of the delay time between the pump and probe photoelectron pulses. The intensity of separate reflections *1*, *2*, and *3* and the integral signal in the sector shown in Fig. 13 were measured. Time scanning of the probe photoelectron pulse with respect to the pump femtosecond laser pulse was performed using a delay line with a step of 60 fs. The signal acquisition time at each step was 1 s. The intensity values measured in this manner were normalized to the intensity of the corresponding reflections in the absence of optical pumping. The results are shown in Fig. 14.

It can be seen that the dynamics observed in Fig. 14 is reproduced well at the detection in all studied regions of the diffraction pattern for the positive time delays corresponding to the arrival of the probe pulse after the pump one. At the excitation time, a sharp decay in the diffraction signal is observed, which is particularly distinct in Fig. 14d. The characteristic time of this decay is about 300 fs. A similar decay was observed in experiments on superfast electron diffraction in bismuth films in the *incoherent* response associated with the Debye–Waller effect owing to the increase in the rms stochastic displacement of atoms after the excitation of the sample [83, 84].

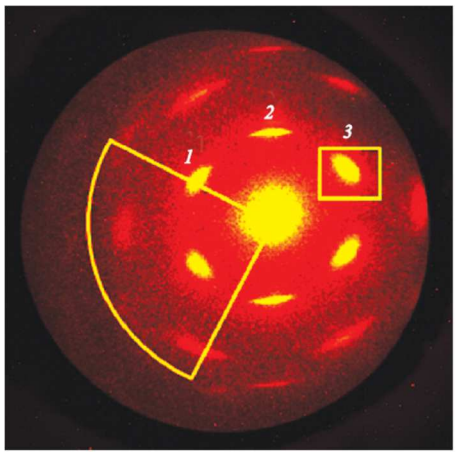

Fig. 13. Electron diffraction pattern of the antimony films (~ 30 nm) obtained using electron photoelectron pulse diffraction. The first, second, and third groups of reflections correspond to the (110), (300), and (220) planes, respectively. The rectangle and sector show the analyzed regions of the diffraction pattern [75]

Рис. 13. Дифракционная картина пленок сурьмы (~ 30 нм), полученных с использованием фотоэлектронной импульсной дифракции электронов. Первая, вторая и третья группы отражений соответствуют плоскостям (110), (300) и (220) соответственно. Прямоугольником и сектором показаны анализируемые области дифракционной картины [75]

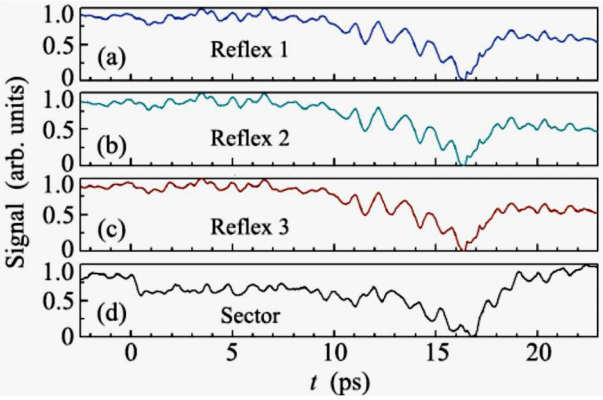

Fig. 14. Normalized relative intensity of electron diffraction reflections in the antimony film versus the delay between the pump optical and probe photoelectron pulses. Curves a–c correspond to reflections 1–3, respectively, in Fig. 13 and the curve d is the sector signal (please, see Fig. 13) [75]

Рис. 14. Зависимость нормированной интенсивности рефлексов электронной дифракции в пленке сурьмы от времени задержки между возбуждающим оптическим и зондирующим фотоэлектронным импульсом. Кривые a–c соответствуют рефлексам 1, 2, 3 на рис.13, кривая d – секторальный сигнал (см. рис. 13) [75]

However, unlike the cited works, along with the rather complicated subsequent dynamics, one can separate the distinct oscillating component with the period on the order of a nanosecond reaching the maximum values and then relaxing in several picoseconds. The Fourier analysis (Fig. 15) showed that the observed signal modulation is due to the presence of four modes with frequencies of 1.1, 3.4, 4.6, and 6.4 THz,

three of which were observed in [78, 79] in experiments on *optical probing* after the impact of a laser pulse with an energy density of ~1 mJ/cm^2 on an antimony sample. Following the attribution of the modes given in these works, it is possible to associate the frequencies of 4.6 and 3.4 THz with the totally symmetric (A_{1g}) and twofold degenerate (E_g) optical phonons of antimony and 1.1 THz with the difference optical vibration A_{1u}–E_g.

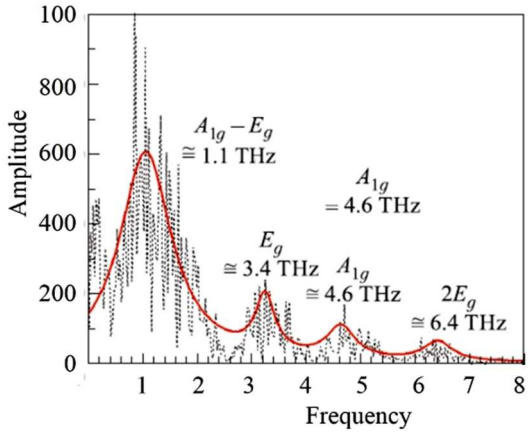

Fig. 15. Fourier spectrum of laser-induced oscillations of the diffraction signal in the antimony film presented in Fig. 26. The dashed line shows the experimental data and the solid line is the Lorentzian fit to the peaks. The frequencies and attribution of the corresponding peaks are also presented. (From ref. [75])

Рис. 15. Фурье-спектр лазерно-индуцированных осцилляций дифракционного сигнала в пленке Sb, представленного на рис. 14. Штриховая линия – эксперимент, сплошная линия – аппроксимация экспериментальных данных функцией Лоренца [75]

The frequency of 6.4 THz for antimony in the time region was not observed earlier. It can be associated with the second harmonic E_g. We note that the pump laser pulse with a duration of 50 fs, the spectrum of which makes it possible to create phonons with frequencies to 7–8 THz, is responsible for the generation of coherent oscillations in our experiment.

The reliable detection of oscillations at the difference frequency with a period of about 1 ps (Fig. 15) makes it possible to state that the time resolution of the performed experiment determined by the electron pulse duration is close to the calculated value. Moreover, the usage of the small step (60 fs) at the time scanning of the photoelectron pulse with a duration of ≈300 fs allowed detecting the frequency of phonons of ≈6.4 THz. The relation of the coherent amplitudes of the main phonon modes and their overtones and/or combinations in our experiment differs from the data of the optical study of the coherent dynamics of the lattice, which can be due both to the specificity of the interaction between fast electrons and nuclei of the lattice and to the time resolution of experiment [75]. It should also be noted that the shape of the signal of coherent phonons in Fig. 17 differs noticeably from that observed earlier in experiments with optical probing [76-79] in the rather significant delay of their "excitation" with respect to the incoherent response. This effect can be explained by the same reasons as the delay of the appearance and the large amplitude of the incoherent signal of the vibrational modes from the surface as compared to the volume in thin bismuth films observed in [84]. At the same time, this problem needs further investigations.

To summarize, the generation of coherent optical phonons in a thin antimony film has been directly observed for the first time using ultrafast electron diffraction. These studies of the coherent dynamics of the antimony lattice indicate that a subpicosecond time resolution has been achieved. This is confirmed by the theoretical estimates and the direct observation of coherent optical phonon modes of antimony with the frequencies varying from 1 to 5-7 THz.

CONCLUDING REMARKS

In 1927, Davisson, Germer [85], independently Thomson, and Reid [86] discovered the phenomenon of electron diffraction in the crystal. This finding pertained to 'static' diffraction. After the first experiments, performed by Mark and Wierl in 1930 [87], the electron diffraction method conceptually remained unchanged until the early 80's. Only 50 years later it became possible to introduce in the fourth dimension in electron diffraction – time, introducing the concepts of structural dynamics, and research in the 4D space–time continuum. Electron diffraction with time resolution opened the possibility of direct observation of processes occurring in the transition state of the substance.

Motion of the atoms can be observed using the time-resolved electron diffraction methods in real time. Rupture of chemical bonds, their formation and change in the geometry of the molecule occur at a rate close to 1000 m/s. Consequently, the registration of the dynamics at the atomic scale, i.e. at distances of the order of angström requires (on average) the temporal resolution of 100 fs. Regardless of the fact that the molecule is isolated or enters the composition of any phase, ultrafast transformations in it are a dynamic process involving the concerted rearrangement of the electron and nuclear subsystems of the reacting molecules. Typical intramolecular fluctuations occur over a time interval of hundreds of femtoseconds. That is why the use of the term 'ultrafast diffraction' is justified to some extent. In this case, it is clear that the diffraction process is determined for electrons by the accelerating voltage and

a single act of scattering occurs in the range of units of attoseconds for electrons with energies of ~100 keV.

The time resolution of about 100 fs was achieved, which corresponds to the transition time of the system through the energy barrier of the potential surface that describes a chemical reaction – the process of breaking and the formation of new bonds of the interacting substances. Thus, it became possible to study the coherent nuclear dynamics of molecular systems and condensed matter. In the past two decades, it became possible to observe the motion of the nuclei in the time interval corresponding to the period of oscillations of the nuclei. The observed coherent changes in the nuclear subsystem in these time intervals determine the fundamental shift from the standard kinetics to the dynamics of the phase trajectory of the single molecule, the tomography of the molecular quantum state.

The effectiveness of both UEC and UEnC has been demonstrated by several groups in the studies of the photo-induced structural homogeneous transitions for the gold nanocrystals [4, 37], in the investigation of the interfacial charge dynamics [88] and in the works on the molecular electronics [89]. Thus, the high sensitivity and high spatio-temporal resolution of these methods give the important opportunity to observe ultrafast processes such as surface melting of the nanoparticles, the non-equilibrium dynamics of the structural phase transitions and the response of the adsorbed molecules on the non-equilibrium structural changes at the surfaces.

Ruan with co-workers studied different Au nanoparticles with their diameters ranging from 2 to 20 nm using UenC [37]. The reversible surface melting and the recrystallization were observed with subpicosecond temporal and a few picometer spatial resolution. In ultrafast photo-induced melting processes under non-equilibrium conditions, the phases of the initial deformation of the lattice, the electron-phonon interaction, the formation of the collective bonds and the disturbance of the atomic coordinations, transforming the nanocrystals in the nanofluids, were established. The structural excitation during pre-melting and coherent transformation from the crystal to the liquid, with the coexistence of different phases during the photomelting, noticeably differ from the re-crystallization process, in which the "hot forms" of the lattice and the liquid phase coexist as a result of their thermal contacts. The degree of the structural changes and the melting thermodynamics was found to be dependent on the size of the nanoparticles [37].

Currently, the method of ultrafast diffraction is being developed intensively. Great opportunities to study the 4D structural dynamics are offered by the methods ultrafast electron crystallography, nanocrystallography, and electron microscopy with time resolution from pico- to femtoseconds.

Acknowledgements. *Support by RFBR grant No. 16-29-1167 OFI_m and partial support by grant No. 15-59-32401 RT-omi.*

ЛИТЕРАТУРА

1. **Ruan C.-Y., Vigliotti F., Lobastov V. A., Chen S., Zewail A. H.** Ultrafast electron crystallography: Transient structures of molecules, surfaces, and phase transitions. *PNAS.* 2004. V. 101. N 5. P. 1123-1128. DOI: 0.1073/pnas.0307302101.
2. **Zewail A. H.** 4D ultrafast electron diffraction, crystallography, and microscopy. *Annu. Rev. Phys. Chem.* 2006. V. 57. N 1. P. 65-103. DOI: 10.1146/annurev.physchem.57.032905.104748.
3. **Dwyer J. R., Hebeisen C. T., Ernstorfer R., Harb M., Deyirmenjian V. B., Jordan R. E., Dwayne Miller R. J.** Femtosecond electron diffraction: 'making the molecular movie'. *Phil. Trans. R. Soc. A.* 2006. V. 364. N 1840. P. 741-778. DOI: 10.1098/rsta.2005.1735.
4. **Ruan C.-Y., Murooka Y., Raman R. K., Murdick R. A., Worhatch R. J., Pell A.** The Development and Applications of Ultrafast Electron Nanocrystallography. *Microsc. Microanal.* 2009. V. 15. N 4. P. 323-337. DOI: 10.1017/s1431927609090709.
5. **Zewail A. H., Thomas J. M.** 4D Electron Microscopy: Imaging in Space and Time. London: Imperial College Press. 2010. 360 p.
6. **Ischenko A. A., Spiridonov V. P., Schäfer L., Ewbank J. D.** The stroboscopic gas electron diffraction method for investigation of time-resolved structural kinetics in photoexcitation processes. *J. Mol. Struct.* 1993. V. 300. P. 115-140. DOI: 10.1016/0022-2860(93)87011-W.

REFERENCES

1. **Ruan C.-Y., Vigliotti F., Lobastov V. A., Chen S., Zewail A. H.** Ultrafast electron crystallography: Transient structures of molecules, surfaces, and phase transitions. *PNAS.* 2004. V. 101. N 5. P. 1123-1128. DOI: 0.1073/pnas.0307302101.
2. **Zewail A. H.** 4D ultrafast electron diffraction, crystallography, and microscopy. *Annu. Rev. Phys. Chem.* 2006. V. 57. N 1. P. 65-103. DOI: 10.1146/annurev.physchem.57.032905.104748.
3. **Dwyer J. R., Hebeisen C. T., Ernstorfer R., Harb M., Deyirmenjian V. B., Jordan R. E., Dwayne Miller R. J.** Femtosecond electron diffraction: 'making the molecular movie'. *Phil. Trans. R. Soc. A.* 2006. V. 364. N 1840. P. 741-778. DOI: 10.1098/rsta.2005.1735.
4. **Ruan C.-Y., Murooka Y., Raman R. K., Murdick R. A., Worhatch R. J., Pell A.** The Development and Applications of Ultrafast Electron Nanocrystallography. *Microsc. Microanal.* 2009. V. 15. N 4. P. 323-337. DOI: 10.1017/s1431927609090709.
5. **Zewail A. H., Thomas J. M.** 4D Electron Microscopy: Imaging in Space and Time. London: Imperial College Press. 2010. 360 p.
6. **Ischenko A. A., Spiridonov V. P., Schäfer L., Ewbank J. D.** The stroboscopic gas electron diffraction method for investigation of time-resolved structural kinetics in photoexcitation processes. *J. Mol. Struct.* 1993. V. 300. P. 115-140. DOI: 10.1016/0022-2860(93)87011-W.

7. **Ishchenko A. A., Bagratashvili V. N., Avilov A. S.** Methods for studying the coherent 4D structural dynamics of free molecules and condensed state of matter. *CryRp*. 2011. V. 56. N 5. P. 751-773. DOI: 10.1134/s1063774511050129.
8. **Ewbank J. D., Schäfer L., Ischenko A. A.** Structural and vibrational kinetics of photoexcitation processes using time resolved electron diffraction. *J. Mol. Struct.* 2000. V. 524. N 1–3. P. 1-49. DOI: 10.1016/S0022-2860(99)00419-6.
9. **Williamson J. C., Cao J., Ihee H., Frey H., Zewail A. H.** Clocking transient chemical changes by ultrafast electron diffraction. *Nature*. 1997. V. 386. N 6621. P. 159-162. DOI: 10.1038/386159a0.
10. **Dudek R. C., Weber P. M.** Ultrafast Diffraction Imaging of the Electrocyclic Ring-Opening Reaction of 1,3-cyclohexadiene. *J. Phys. Chem. A*. 2001. V. 105. N 17. P. 4167-4171. DOI: 10.1021/jp010122t.
11. **Srinivasan R., Lobastov V. A., Ruan C.-Y., Zewail A. H.** Ultrafast Electron Diffraction (UED). *Helv. Chim. Acta*. 2003. V. 86. N 6. P. 1761-1799. DOI: 10.1002/hlca.200390147.
12. **Sciaini G., Dwayne Miller R. J.** Femtosecond electron diffraction: heralding the era of atomically resolved dynamics. *Rep. Prog. Phys.* 2011. V. 74. N 9. P. 096101, 1-36. DOI: 10.1088/0034-4885/74/9/096101.
13. **Lobastov V. A., Srinivasan R., Vigliotti F., Ruan C.-Y., Feenstra J. S., Chen S., Park S. T., Xu S., Zewail A. H.** Ultrafast Electron Diffraction, in: Ultrafast Optics IV: Selected Contributions to the 4th International Conference on Ultrafast Optics, 2004. New York: Springer. P. 419-435.
14. **Lobastov V. A., Srinivasan R., Zewail A. H.** Four-dimensional ultrafast electron microscopy. *PNAS*. 2005. V. 102. N 20. P. 7069-7073. DOI: 10.1073/pnas.0502607102.
15. **King W. E., Campbell G. H., Frank A., Reed B., Schmerge J. F., Siwick B. J., Stuart B. C., Weber P. M.** Ultrafast electron microscopy in materials science, biology, and chemistry. *J. Appl. Phys.* 2005. V. 97. N 11. P. 111101, 1-27. DOI: 10.1063/1.1927699.
16. **Ищенко А.А., Шефер Л., Тарасов Ю.И., Рябов Е.А., Асеев С.А.** Сверхбыстрая просвечивающая электронная микроскопия. *Тонкие химические технологии*. 2017. Т. 12. Вып. 1. С. 5-25.
17. **Шефер Л., Тарасов Ю.И., Кошелев А.В., Ищенко А.А.** Сверхбыстрая электронная кристаллография и нанокристаллография: для химии, биологии и наук о материалах. Часть I. Сверхбыстрая электронная кристаллография. *Изв. вузов. Химия и хим. технология*. 2017. Т. 60. Вып. 5. С. 4-20. DOI: 10.6060/tcct.2017605.5608.
18. **Ino S., Ogawa S.** Multiply Twinned Particles at Earlier Stages of Gold Film Formation on Alkalihalide Crystals. *J. Phys. Soc. Japan*. 1967. V. 22. N 6. P. 1365-1374. DOI: 10.1143/jpsj.22.1365.
19. **Wales D. J.** Structure, Dynamics, and Thermodynamics of Clusters: Tales from Topographic Potential Surfaces. *Science*. 1996. V. 271. N 5251. P. 925-929. DOI: 10.1126/science.271.5251.925.
20. **Mackay A.** A dense non-crystallographic packing of equal spheres. *Acta Cryst*. 1962. V. 15. N 9. P. 916-918. DOI: 10.1107/s0365110x6200239x.
21. **Eberhardt W.** Clusters as new materials. *Surface Science*. 2002. V. 500. N 1. P. 242-270. DOI: 10.1016/S0039-6028(01)01564-3.
22. **Ищенко А.А., Фетисов Г.В., Асланов Л.А.** Нанокремний: свойства, получение, применение, методы исследования и контроля. М.: Физматлит. 2011. 646 с.

7. **Ishchenko A. A., Bagratashvili V. N., Avilov A. S.** Methods for studying the coherent 4D structural dynamics of free molecules and condensed state of matter. *CryRp*. 2011. V. 56. N 5. P. 751-773. DOI: 10.1134/s1063774511050129.
8. **Ewbank J. D., Schäfer L., Ischenko A. A.** Structural and vibrational kinetics of photoexcitation processes using time resolved electron diffraction. *J. Mol. Struct.* 2000. V. 524. N 1–3. P. 1-49. DOI: 10.1016/S0022-2860(99)00419-6.
9. **Williamson J. C., Cao J., Ihee H., Frey H., Zewail A. H.** Clocking transient chemical changes by ultrafast electron diffraction. *Nature*. 1997. V. 386. N 6621. P. 159-162. DOI: 10.1038/386159a0.
10. **Dudek R. C., Weber P. M.** Ultrafast Diffraction Imaging of the Electrocyclic Ring-Opening Reaction of 1,3-cyclohexadiene. *J. Phys. Chem. A*. 2001. V. 105. N 17. P. 4167-4171. DOI: 10.1021/jp010122t.
11. **Srinivasan R., Lobastov V. A., Ruan C.-Y., Zewail A. H.** Ultrafast Electron Diffraction (UED). *Helv. Chim. Acta*. 2003. V. 86. N 6. P. 1761-1799. DOI: 10.1002/hlca.200390147.
12. **Sciaini G., Dwayne Miller R. J.** Femtosecond electron diffraction: heralding the era of atomically resolved dynamics. *Rep. Prog. Phys.* 2011. V. 74. N 9. P. 096101, 1-36. DOI: 10.1088/0034-4885/74/9/096101.
13. **Lobastov V. A., Srinivasan R., Vigliotti F., Ruan C.-Y., Feenstra J. S., Chen S., Park S. T., Xu S., Zewail A. H.** Ultrafast Electron Diffraction, in: Ultrafast Optics IV: Selected Contributions to the 4th International Conference on Ultrafast Optics, 2004. New York: Springer. P. 419-435.
14. **Lobastov V. A., Srinivasan R., Zewail A. H.** Four-dimensional ultrafast electron microscopy. *PNAS*. 2005. V. 102. N 20. P. 7069-7073. DOI: 10.1073/pnas.0502607102.
15. **King W. E., Campbell G. H., Frank A., Reed B., Schmerge J. F., Siwick B. J., Stuart B. C., Weber P. M.** Ultrafast electron microscopy in materials science, biology, and chemistry. *J. Appl. Phys.* 2005. V. 97. N 11. P. 111101, 1-27. DOI: 10.1063/1.1927699.
16. **Ischenko A. A., Schaefer L., Tarasov Y. I., Ryabov E. A., Aseyev S. A.** Ultrafast Transmission Electron Microscopy. *Tonkie Khim. Tekhnol.* 2017. V. 12. N 1. P. 5-25 (in Russian).
17. **Schafer L., Tarasov Y. I., Koshelev A. V., Ischenko A. A.** Ultrafast Electron Crystallography and Nanocrystallography: for Chemistry, Biology and Materials Science. Part I. Ultrafast Electron Crystallography. *Izv. Vyssh. Uchebn. Zaved. Khim. Khim. Tekhnol.* 2017. V. 60. N 5. P. 4-20. DOI: 10.6060/tcct.2017605.5608.
18. **Ino S., Ogawa S.** Multiply Twinned Particles at Earlier Stages of Gold Film Formation on Alkalihalide Crystals. *J. Phys. Soc. Japan*. 1967. V. 22. N 6. P. 1365-1374. DOI: 10.1143/jpsj.22.1365.
19. **Wales D. J.** Structure, Dynamics, and Thermodynamics of Clusters: Tales from Topographic Potential Surfaces. *Science*. 1996. V. 271. N 5251. P. 925-929. DOI: 10.1126/science.271.5251.925.
20. **Mackay A.** A dense non-crystallographic packing of equal spheres. *Acta Cryst*. 1962. V. 15. N 9. P. 916-918. DOI: 10.1107/s0365110x6200239x.
21. **Eberhardt W.** Clusters as new materials. *Surface Science*. 2002. V. 500. N 1. P. 242-270. DOI: 10.1016/S0039-6028(01)01564-3.
22. **Ischenko A. A., Fetisov G. V., Aslanov L. A.** Nanosilicon: properties, synthesis, applications, methods of analysis and control. Moscow: FIZMATLIT. 2011. 646 p. (in Russian).

23. **Whetten R. L., Khoury J. T., Alvarez M. M., Murthy S., Vezmar I., Wang Z. L., Stephens P. W., Cleveland C. L., Luedtke W. D., Landman U.** Nanocrystal gold molecules. *Adv. Mater*. 1996. V. 8. N 5. P. 428-433. DOI: 10.1002/adma.19960080513.
24. **Zanchet D., Tolentino H., Martins Alves M. C., Alves O. L., Ugarte D.** Inter-atomic distance contraction in thiol-passivated gold nanoparticles. *Chem. Phys. Lett.* 2000. V. 323. N 1–2. P. 167-172. DOI: 10.1016/S0009-2614(00)00424-3.
25. **Marks L. D.** Experimental studies of small particle structures. *Rep. Prog. Phys.* 1994. V. 57. N 6. P. 603-649. DOI: 10.1088/0034-4885/57/6/002.
26. **Klein D. L., McEuen P. L., Bowen Katari J. E., Roth R., Paul Alivisatos A.** An approach to electrical studies of single nanocrystals. *Appl. Phys. Lett*. 1996. V. 68. N 18. P. 2574-2576. DOI: 10.1063/1.116188.
27. **Alivisatos A. P.** Semiconductor Clusters, Nanocrystals, and Quantum Dots. *Science*. 1996. V. 271. N 5251. P. 933-937. DOI: 10.1126/science.271.5251.933.
28. **Awschalom D. D., DiVincenzo D. P., Smyth J. F.** Macroscopic Quantum Effects in Nanometer-Scale Magnets. *Science*. 1992. V. 258. N 5081. P. 414-421. DOI: 10.1126/science.258.5081.414.
29. **Haruta M.** Size- and support-dependency in the catalysis of gold. *Catal. Today*. 1997. V. 36. N 1. P. 153-166. DOI: 10.1016/S0920-5861(96)00208-8.
30. **Häkkinen H., Abbet S., Sanchez A., Heiz U., Landman U.** Structural, Electronic, and Impurity-Doping Effects in Nanoscale Chemistry: Supported Gold Nanoclusters. *Angew. Chem. Int. Ed*. 2003. V. 42. N 11. P. 1297-1300. DOI: 10.1002/anie.200390334.
31. **Shipway A. N., Katz E., Willner I.** Nanoparticle Arrays on Surfaces for Electronic, Optical, and Sensor Applications. Phys. *Chem.Chem.Phys* 2000. V. 1. N 1. P. 18-52. DOI: 10.1002/1439-7641(20000804)1:1<18::aid-cphc18>3.0.co;2-l.
32. **Siwick B. J., Dwyer J. R., Jordan R. E., Dwayne Miller R. J.** An Atomic-Level View of Melting Using Femtosecond Electron Diffraction. *Science*. 2003. V. 302. N 5649. P. 1382-1385. DOI: 10.1126/science.1090052.
33. **Cao J., Hao Z., Park H., Tao C., Kau D., Blaszczyk L.** Femtosecond electron diffraction for direct measurement of ultrafast atomic motions. *Appl. Phys. Lett.* 2003. V. 83. N 5. P. 1044-1046. DOI: 10.1063/1.1593831.
34. **Anderson S. G., Musumeci P., Rosenzweig J. B., Brown W. J., England R. J., Ferrario M., Jacob J. S., Thompson M. C., Travish G., Tremaine A. M., Yoder R.** Velocity bunching of high-brightness electron beams. *Phys. Rev. Accel. Beams*. 2005. V. 8. N 1. P. 014401, 1-22. DOI: 10.1103/PhysRevSTAB.8.014401.
35. **van Oudheusden T., de Jong E. F., van den Geer S. B., Op't Root W. P. E. M., Luiten O. J., Siwick B. J.** Electron source concept for single-shot sub-100 fs electron diffraction in the 100 keV range. *J. Appl. Phys.* 2007. V. 102. N 9. P. 093501. DOI: 10.1063/1.2801027.
36. **Hommelhoff P., Sortais Y., Aghajani-Talesh A., Kasevich M. A.** Field Emission Tip as a Nanometer Source of Free Electron Femtosecond Pulses. *Phys. Rev. Lett.* 2006. V. 96. N 7. P. 077401. DOI: 10.1103/PhysRevLett.96.077401.
37. **Ruan C.-Y., Murooka Y., Raman R. K., Murdick R. A.** Dynamics of Size-Selected Gold Nanoparticles Studied by Ultrafast Electron Nanocrystallography. *Nano Letters*. 2007. V. 7. N 5. P. 1290-1296. DOI: 10.1021/nl070269h.

23. **Whetten R. L., Khoury J. T., Alvarez M. M., Murthy S., Vezmar I., Wang Z. L., Stephens P. W., Cleveland C. L., Luedtke W. D., Landman U.** Nanocrystal gold molecules. *Adv. Mater*. 1996. V. 8. N 5. P. 428-433. DOI: 10.1002/adma.19960080513.
24. **Zanchet D., Tolentino H., Martins Alves M. C., Alves O. L., Ugarte D.** Inter-atomic distance contraction in thiol-passivated gold nanoparticles. *Chem. Phys. Lett.* 2000. V. 323. N 1–2. P. 167-172. DOI: 10.1016/S0009-2614(00)00424-3.
25. **Marks L. D.** Experimental studies of small particle structures. *Rep. Prog. Phys.* 1994. V. 57. N 6. P. 603-649. DOI: 10.1088/0034-4885/57/6/002.
26. **Klein D. L., McEuen P. L., Bowen Katari J. E., Roth R., Paul Alivisatos A.** An approach to electrical studies of single nanocrystals. *Appl. Phys. Lett.* 1996. V. 68. N 18. P. 2574-2576. DOI: 10.1063/1.116188.
27. **Alivisatos A. P.** Semiconductor Clusters, Nanocrystals, and Quantum Dots. *Science*. 1996. V. 271. N 5251. P. 933-937. DOI: 10.1126/science.271.5251.933.
28. **Awschalom D. D., DiVincenzo D. P., Smyth J. F.** Macroscopic Quantum Effects in Nanometer-Scale Magnets. *Science*. 1992. V. 258. N 5081. P. 414-421. DOI: 10.1126/science.258.5081.414.
29. **Haruta M.** Size- and support-dependency in the catalysis of gold. *Catal. Today*. 1997. V. 36. N 1. P. 153-166. DOI: 10.1016/S0920-5861(96)00208-8.
30. **Häkkinen H., Abbet S., Sanchez A., Heiz U., Landman U.** Structural, Electronic, and Impurity-Doping Effects in Nanoscale Chemistry: Supported Gold Nanoclusters. *Angew. Chem. Int. Ed*. 2003. V. 42. N 11. P. 1297-1300. DOI: 10.1002/anie.200390334.
31. **Shipway A. N., Katz E., Willner I.** Nanoparticle Arrays on Surfaces for Electronic, Optical, and Sensor Applications. Phys.*Chem.Chem.Phys.* 2000. V. 1. N 1. P. 18-52. DOI: 10.1002/1439-7641(20000804)1:1<18::aid-cphc18>3.0.co;2-l.
32. **Siwick B. J., Dwyer J. R., Jordan R. E., Dwayne Miller R. J.** An Atomic-Level View of Melting Using Femtosecond Electron Diffraction. *Science*. 2003. V. 302. N 5649. P. 1382-1385. DOI: 10.1126/science.1090052.
33. **Cao J., Hao Z., Park H., Tao C., Kau D., Blaszczyk L.** Femtosecond electron diffraction for direct measurement of ultrafast atomic motions. *Appl. Phys. Lett.* 2003. V. 83. N 5. P. 1044-1046. DOI: 10.1063/1.1593831.
34. **Anderson S. G., Musumeci P., Rosenzweig J. B., Brown W. J., England R. J., Ferrario M., Jacob J. S., Thompson M. C., Travish G., Tremaine A. M., Yoder R.** Velocity bunching of high-brightness electron beams. *Phys. Rev. Accel. Beams*. 2005. V. 8. N 1. P. 014401, 1-22. DOI: 10.1103/PhysRevSTAB.8.014401.
35. **van Oudheusden T., de Jong E. F., van den Geer S. B., Op't Root W. P. E. M., Luiten O. J., Siwick B. J.** Electron source concept for single-shot sub-100 fs electron diffraction in the 100 keV range. *J. Appl. Phys.* 2007. V. 102. N 9. P. 093501. DOI: 10.1063/1.2801027.
36. **Hommelhoff P., Sortais Y., Aghajani-Talesh A., Kasevich M. A.** Field Emission Tip as a Nanometer Source of Free Electron Femtosecond Pulses. *Phys. Rev. Lett.* 2006. V. 96. N 7. P. 077401. DOI: 10.1103/PhysRevLett.96.077401.
37. **Ruan C.-Y., Murooka Y., Raman R. K., Murdick R. A.** Dynamics of Size-Selected Gold Nanoparticles Studied by Ultrafast Electron Nanocrystallography. *Nano Letters*. 2007. V. 7. N 5. P. 1290-1296. DOI: 10.1021/nl070269h.

38. **Sato T., Ahmed H., Brown D., Johnson B. F. G.** Single electron transistor using a molecularly linked gold colloidal particle chain. *J. Appl. Phys.* 1997. V. 82. N 2. P. 696-701. DOI: 10.1063/1.365600.
39. **Оура К., Лифшиц В.Г., Саранин А.А., Зотов А.В., Катаяма М**. Введение в физику поверхности. М.: Наука. 2006. 494 с.
40. **Kern W., Puotinen D. A.** Cleaning Solution-based on hydrogen peroxide for use in silicon semiconductor technology. *RCA Rev.* 1970. V. 31. N 2. P. 187-206.
41. **Schmitt J., Mächtle P., Eck D., Möhwald H., Helm C. A.** Preparation and Optical Properties of Colloidal Gold Monolayers. *Langmuir*. 1999. V. 15. N 9. P. 3256-3266. DOI: 10.1021/la981078k.
42. **Liu S., Zhu T., Hu R., Liu Z.** Evaporation-induced self-assembly of gold nanoparticles into a highly organized two-dimensional array. *Phys. Chem. Chem. Phys.* 2002. V. 4. N 24. P. 6059-6062. DOI: 10.1039/b208520h.
43. **Bhat R. R., Fischer D. A., Genzer J.** Fabricating Planar Nanoparticle Assemblies with Number Density Gradients. *Langmuir*. 2002. V. 18. N 15. P. 5640-5643. DOI: 10.1021/la025524m.
44. **Westcott S. L., Oldenburg S. J., Lee T. R., Halas N. J.** Formation and Adsorption of Clusters of Gold Nanoparticles onto Functionalized Silica Nanoparticle Surfaces. *Langmuir*. 1998. V. 14. N 19. P. 5396-5401. DOI: 10.1021/la980380q
45. **Warren B. E.** X-ray Diffraction. New York: Dover Publications, Inc. 1990. 400 p.
46. **Doyle P. A., Turner P. S.** Relativistic Hartree-Fock X-ray and electron scattering factors. *Acta Crystallogr. Sect. A.* 1968. V. 24. N 3. P. 390-397. DOI: DOI:10.1107/S0567739468000756.
47. **Peng L. M., Dudarev S. L., Whelan M. J.** High energy electron diffraction and microscopy. Oxford: Oxford University Press. 2004. p.
48. **Dwayne Miller R. J.** Femtosecond Crystallography with Ultrabright Electrons and X-rays: Capturing Chemistry in Action. *Science*. 2014. V. 343. N 6175. P. 1108-1116. DOI: 10.1126/science.1248488.
49. **Born M.** Thermodynamics of Crystals and Melting. *J. Chem. Phys.* 1939. V. 7. N 8. P. 591-603. DOI: 10.1063/1.1750497.
50. **Ernstorfer R., Harb M., Hebeisen C. T., Sciaini G., Dartigalongue T., Dwayne Miller R. J.** The Formation of Warm Dense Matter: Experimental Evidence for Electronic Bond Hardening in Gold. *Science*. 2009. V. 323. N 5917. P. 1033-1037. DOI: 10.1126/science.1162697.
51. **Dwayne Miller R. J.** Mapping Atomic Motions with Ultrabright Electrons: The Chemists' Gedanken Experiment Enters the Lab Frame. *Annu. Rev. Phys. Chem.* 2014. V. 65. N 1. P. 583-604. DOI: 10.1146/annurev-physchem-040412-110117.
52. **Erasmus N., Eichberger M., Haupt K., Boshoff I., Kassier G., Birmurske R., Berger H., Demsar J., Schwoerer H.** Ultrafast Dynamics of Charge Density Waves in $4H_b$-$TaSe_2$ Probed by Femtosecond Electron Diffraction. *Phys. Rev. Lett.* 2012. V. 109. N 16. P. 167402. DOI: 10.1103/PhysRevLett.109.167402.
53. **Lin Z., Zhigilei L. V.** Time-resolved diffraction profiles and atomic dynamics in short-pulse laser-induced structural transformations: Molecular dynamics study. *Phys. Rev. B.* 2006. V. 73. N 18. P. 184113. DOI: 10.1103/PhysRevB.73.184113.
54. **Amini-Nik S., Kraemer D., Cowan M. L., Gunaratne K., Nadesan P., Alman B. A., Dwayne Miller R. J.** Ultrafast Mid-IR Laser Scalpel: Protein Signals of the Fundamental Limits to Minimally Invasive Surgery. *PLoS ONE*. 2010. V. 5. N 9. P. e13053. DOI: 10.1371/journal.pone.0013053.

38. **Sato T., Ahmed H., Brown D., Johnson B. F. G.** Single electron transistor using a molecularly linked gold colloidal particle chain. *J. Appl. Phys.* 1997. V. 82. N 2. P. 696-701. DOI: 10.1063/1.365600.

39. **Oura K., Lifshits V. G., Saranin A. A., Zotov A. V., Katayama M.** Introduction to the physics of the surface. Moscow: Nauka. 2006. 494 p. (in Russian).

40. **Kern W., Puotinen D. A.** Cleaning Solution-based on hydrogen peroxide for use in silicon semiconductor technology. *RCA Rev.* 1970. V. 31. N 2. P. 187-206.
41. **Schmitt J., Mächtle P., Eck D., Möhwald H., Helm C. A.** Preparation and Optical Properties of Colloidal Gold Monolayers. *Langmuir*. 1999. V. 15. N 9. P. 3256-3266. DOI: 10.1021/la981078k.
42. **Liu S., Zhu T., Hu R., Liu Z.** Evaporation-induced self-assembly of gold nanoparticles into a highly organized two-dimensional array. *Phys. Chem. Chem. Phys.* 2002. V. 4. N 24. P. 6059-6062. DOI: 10.1039/b208520h.
43. **Bhat R. R., Fischer D. A., Genzer J.** Fabricating Planar Nanoparticle Assemblies with Number Density Gradients. *Langmuir*. 2002. V. 18. N 15. P. 5640-5643. DOI: 10.1021/la025524m.
44. **Westcott S. L., Oldenburg S. J., Lee T. R., Halas N. J.** Formation and Adsorption of Clusters of Gold Nanoparticles onto Functionalized Silica Nanoparticle Surfaces. *Langmuir*. 1998. V. 14. N 19. P. 5396-5401. DOI: 10.1021/la980380q
45. **Warren B. E.** X-ray Diffraction. New York: Dover Publications, Inc. 1990. 400 p.
46. **Doyle P. A., Turner P. S.** Relativistic Hartree-Fock X-ray and electron scattering factors. *Acta Crystallogr. Sect. A.* 1968. V. 24. N 3. P. 390-397. DOI: DOI:10.1107/S0567739468000756.
47. **Peng L. M., Dudarev S. L., Whelan M. J.** High energy electron diffraction and microscopy. Oxford: Oxford University Press. 2004. p.
48. **Dwayne Miller R. J.** Femtosecond Crystallography with Ultrabright Electrons and X-rays: Capturing Chemistry in Action. *Science*. 2014. V. 343. N 6175. P. 1108-1116. DOI: 10.1126/science.1248488.
49. **Born M.** Thermodynamics of Crystals and Melting. *J. Chem. Phys.* 1939. V. 7. N 8. P. 591-603. DOI: 10.1063/1.1750497.
50. **Ernstorfer R., Harb M., Hebeisen C. T., Sciaini G., Dartigalongue T., Dwayne Miller R. J.** The Formation of Warm Dense Matter: Experimental Evidence for Electronic Bond Hardening in Gold. *Science*. 2009. V. 323. N 5917. P. 1033-1037. DOI: 10.1126/science.1162697.
51. **Dwayne Miller R. J.** Mapping Atomic Motions with Ultrabright Electrons: The Chemists' Gedanken Experiment Enters the Lab Frame. *Annu. Rev. Phys. Chem.* 2014. V. 65. N 1. P. 583-604. DOI: 10.1146/annurev-physchem-040412-110117.
52. **Erasmus N., Eichberger M., Haupt K., Boshoff I., Kassier G., Birmurske R., Berger H., Demsar J., Schwoerer H.** Ultrafast Dynamics of Charge Density Waves in $4H_b$-$TaSe_2$ Probed by Femtosecond Electron Diffraction. *Phys. Rev. Lett.* 2012. V. 109. N 16. P. 167402. DOI: 10.1103/PhysRevLett.109.167402.
53. **Lin Z., Zhigilei L. V.** Time-resolved diffraction profiles and atomic dynamics in short-pulse laser-induced structural transformations: Molecular dynamics study. *Phys. Rev. B.* 2006. V. 73. N 18. P. 184113. DOI: 10.1103/PhysRevB.73.184113.
54. **Amini-Nik S., Kraemer D., Cowan M. L., Gunaratne K., Nadesan P., Alman B. A., Dwayne Miller R. J.** Ultrafast Mid-IR Laser Scalpel: Protein Signals of the Fundamental Limits to Minimally Invasive Surgery. *PLoS ONE*. 2010. V. 5. N 9. P. e13053. DOI: 10.1371/journal.pone.0013053.

55. **Harb M., Ernstorfer R., Hebeisen C. T., Sciaini G., Peng W., Dartigalongue T., Eriksson M. A., Lagally M. G., Kruglik S. G., Dwayne Miller R. J.** Electronically Driven Structure Changes of Si Captured by Femtosecond Electron Diffraction. *Phys. Rev. Lett.* 2008. V. 100. N 15. P. 155504. DOI: 10.1103/PhysRevLett.100.155504.
56. **Sciaini G., Harb M., Kruglik S. G., Payer T., Hebeisen C. T., Heringdorf F.-J. M. z., Yamaguchi M., Hoegen M. H.-v., Ernstorfer R., Dwayne Miller R. J.** Electronic acceleration of atomic motions and disordering in bismuth. *Nature*. 2009. V. 458. N 7234. P. 56-59. DOI: 10.1038/nature07788.
57. **Eichberger M., Schafer H., Krumova M., Beyer M., Demsar J., Berger H., Moriena G., Sciaini G., Dwayne Miller R. J.** Snapshots of cooperative atomic motions in the optical suppression of charge density waves. *Nature*. 2010. V. 468. N 7325. P. 799-802. DOI: 10.1038/nature09539.
58. **Han T.-R. T., Tao Z., Mahanti S. D., Chang K., Ruan C.-Y., Malliakas C. D., Kanatzidis M. G.** Structural dynamics of two-dimensional charge-density waves in $CeTe_3$ investigated by ultrafast electron crystallography. *Phys. Rev. B.* 2012. V. 86. N 7. P. 075145. DOI: 10.1103/PhysRevB.86.075145.
59. **Gao M., Lu C., Jean-Ruel H., Liu L. C., Marx A., Onda K., Koshihara S.-y., Nakano Y., Shao X., Hiramatsu T., Saito G., Yamochi H., Cooney R. R., Moriena G., Sciaini G., Dwayne Miller R. J.** Mapping molecular motions leading to charge delocalization with ultrabright electrons. *Nature*. 2013. V. 496. N 7445. P. 343-346. DOI: 10.1038/nature12044.
60. **Jean-Ruel H., Gao M., Kochman M. A., Lu C., Liu L. C., Cooney R. R., Morrison C. A., Dwayne Miller R. J.** Ring-Closing Reaction in Diarylethene Captured by Femtosecond Electron Crystallography. *J. Phys. Chem. B.* 2013. V. 117. N 49. P. 15894-15902. DOI: 10.1021/jp409245h.
61. **Iijima S., Ichihashi T.** Structural instability of ultrafine particles of metals. *Phys. Rev. Lett.* 1986. V. 56. N 6. P. 616-619. DOI: 10.1103/PhysRevLett.56.616.
62. **Ercolessi F., Andreoni W., Tosatti E.** Melting of small gold particles: Mechanism and size effects. *Phys. Rev. Lett.* 1991. V. 66. N 7. P. 911-914. DOI: 10.1103/PhysRevLett.66.911.
63. **Williams P.** Motion of small gold clusters in the electron microscope. *Appl. Phys. Lett.* 1987. V. 50. N 24. P. 1760-1762. DOI: 10.1063/1.97739.
64. **Link S., El-Sayed M. A.** Spectroscopic determination of the melting energy of a gold nanorod. *J. Chem. Phys.* 2001. V. 114. N 5. P. 2362-2368. DOI: 10.1063/1.1336140.
65. **Plech A., Kotaidis V., Grésillon S., Dahmen C., von Plessen G.** Laser-induced heating and melting of gold nanoparticles studied by time-resolved x-ray scattering. *Phys. Rev. B.* 2004. V. 70. N 19. P. 195423. DOI: 10.1103/PhysRevB.70.195423.
66. **Hartland G. V., Hu M., Sader J. E.** Softening of the Symmetric Breathing Mode in Gold Particles by Laser-Induced Heating. *J. Phys. Chem. B.* 2003. V. 107. N 30. P. 7472-7478. DOI: 10.1021/jp0276092.
67. **Plech A., Cerna R., Kotaidis V., Hudert F., Bartels A., Dekorsy T.** A Surface Phase Transition of Supported Gold Nanoparticles. *Nano Lett*. 2007. V. 7. N 4. P. 1026-1031. DOI: 10.1021/nl070187t.
68. **Lewis L. J., Jensen P., Barrat J.-L.** Melting, freezing, and coalescence of gold nanoclusters. *Phys. Rev. B.* 1997. V. 56. N 4. P. 2248-2257. DOI: 10.1103/PhysRevB.56.2248.

55. **Harb M., Ernstorfer R., Hebeisen C. T., Sciaini G., Peng W., Dartigalongue T., Eriksson M. A., Lagally M. G., Kruglik S. G., Dwayne Miller R. J.** Electronically Driven Structure Changes of Si Captured by Femtosecond Electron Diffraction. *Phys. Rev. Lett.* 2008. V. 100. N 15. P. 155504. DOI: 10.1103/PhysRevLett.100.155504.
56. **Sciaini G., Harb M., Kruglik S. G., Payer T., Hebeisen C. T., Heringdorf F.-J. M. z., Yamaguchi M., Hoegen M. H.-v., Ernstorfer R., Dwayne Miller R. J.** Electronic acceleration of atomic motions and disordering in bismuth. *Nature*. 2009. V. 458. N 7234. P. 56-59. DOI: 10.1038/nature07788.
57. **Eichberger M., Schafer H., Krumova M., Beyer M., Demsar J., Berger H., Moriena G., Sciaini G., Dwayne Miller R. J.** Snapshots of cooperative atomic motions in the optical suppression of charge density waves. *Nature*. 2010. V. 468. N 7325. P. 799-802. DOI: 10.1038/nature09539.
58. **Han T.-R. T., Tao Z., Mahanti S. D., Chang K., Ruan C.-Y., Malliakas C. D., Kanatzidis M. G.** Structural dynamics of two-dimensional charge-density waves in $CeTe_3$ investigated by ultrafast electron crystallography. *Phys. Rev. B.* 2012. V. 86. N 7. P. 075145. DOI: 10.1103/PhysRevB.86.075145.
59. **Gao M., Lu C., Jean-Ruel H., Liu L. C., Marx A., Onda K., Koshihara S.-y., Nakano Y., Shao X., Hiramatsu T., Saito G., Yamochi H., Cooney R. R., Moriena G., Sciaini G., Dwayne Miller R. J.** Mapping molecular motions leading to charge delocalization with ultrabright electrons. *Nature*. 2013. V. 496. N 7445. P. 343-346. DOI: 10.1038/nature12044.
60. **Jean-Ruel H., Gao M., Kochman M. A., Lu C., Liu L. C., Cooney R. R., Morrison C. A., Dwayne Miller R. J.** Ring-Closing Reaction in Diarylethene Captured by Femtosecond Electron Crystallography. *J. Phys. Chem. B.* 2013. V. 117. N 49. P. 15894-15902. DOI: 10.1021/jp409245h.
61. **Iijima S., Ichihashi T.** Structural instability of ultrafine particles of metals. *Phys. Rev. Lett.* 1986. V. 56. N 6. P. 616-619. DOI: 10.1103/PhysRevLett.56.616.
62. **Ercolessi F., Andreoni W., Tosatti E.** Melting of small gold particles: Mechanism and size effects. *Phys. Rev. Lett.* 1991. V. 66. N 7. P. 911-914. DOI: 10.1103/PhysRevLett.66.911.
63. **Williams P.** Motion of small gold clusters in the electron microscope. *Appl. Phys. Lett.* 1987. V. 50. N 24. P. 1760-1762. DOI: 10.1063/1.97739.
64. **Link S., El-Sayed M. A.** Spectroscopic determination of the melting energy of a gold nanorod. *J. Chem. Phys.* 2001. V. 114. N 5. P. 2362-2368. DOI: 10.1063/1.1336140.
65. **Plech A., Kotaidis V., Grésillon S., Dahmen C., von Plessen G.** Laser-induced heating and melting of gold nanoparticles studied by time-resolved x-ray scattering. *Phys. Rev. B.* 2004. V. 70. N 19. P. 195423. DOI: 10.1103/PhysRevB.70.195423.
66. **Hartland G. V., Hu M., Sader J. E.** Softening of the Symmetric Breathing Mode in Gold Particles by Laser-Induced Heating. *J. Phys. Chem. B.* 2003. V. 107. N 30. P. 7472-7478. DOI: 10.1021/jp0276092.
67. **Plech A., Cerna R., Kotaidis V., Hudert F., Bartels A., Dekorsy T.** A Surface Phase Transition of Supported Gold Nanoparticles. *Nano Lett*. 2007. V. 7. N 4. P. 1026-1031. DOI: 10.1021/nl070187t.
68. **Lewis L. J., Jensen P., Barrat J.-L.** Melting, freezing, and coalescence of gold nanoclusters. *Phys. Rev. B.* 1997. V. 56. N 4. P. 2248-2257. DOI: 10.1103/PhysRevB.56.2248.

69. **Raman R. K., Murooka Y., Ruan C.-Y., Yang T., Berber S., Tománek D.** Direct Observation of Optically Induced Transient Structures in Graphite Using Ultrafast Electron Crystallography. *Phys. Rev. Lett.* 2008. V. 101. N 7. P. 077401. DOI: 10.1103/PhysRevLett.101.077401.
70. **Touloukian Y. S., Kirby R. K., Taylor R. E., Desai P. D.** Thermal expansion: Metallic elements and alloys. Boston, MA: Springer US. 1975. 1440 p.
71. **Buffat P., Borel J. P.** Size effect on the melting temperature of gold particles. *Phys. Rev. A*. 1976. V. 13. N 6. P. 2287-2298. DOI: 10.1103/PhysRevA.13.2287.
72. **Wang N., Rokhlin S. I., Farson D. F.** Nonhomogeneous surface premelting of Au nanoparticles. *Nanotechnology*. 2008. V. 19. N 41. P. 415701. DOI: 10.1088/0957-4484/19/41/415701.
73. **Billinge S. J. L., Levin I.** The Problem with Determining Atomic Structure at the Nanoscale. *Science*. 2007. V. 316. N 5824. P. 561-565. DOI: 10.1126/science.1135080.
74. **McGreevy R. L.** Reverse Monte Carlo modelling. *J. Phys. Condens. Matter*. 2001. V. 13. N 46. P. R877-R913.
75. **Mironov B. N., Kompanets V. O., Aseev S. A., Ishchenko A. A., Misochko O. V., Chekalin S. V., Ryabov E. A.** Direct observation of the generation of coherent optical phonons in thin antimony films by the femtosecond electron diffraction method. *JETP Letters*. 2016. V. 103. N 8. P. 531-534. DOI: 10.1134/s0021364016080099.
76. **Mel'nikov A.A., Misochko O.V., Chekalin S.V.** Investigation of coherent phonons in bismuth by femtosecond laser and X-ray pulse probing. *JETP Letters*. 2009. V. 89. N 3. P. 129-132. DOI: 10.1134/s0021364009030072.
77. **Misochko O. V., Ishioka K., Hase M., Kitajima M.** Fully symmetric and doubly degenerate coherent phonons in semimetals at low temperature and high excitation: similarities and differences. *J. Phys. Condens. Matter*. 2006. V. 18. N 47. P. 10571-10584.
78. **Ishioka K., Kitajima M., Misochko O. V.** Coherent A1g and Eg phonons of antimony. *J. Appl. Phys.* 2008. V. 103. N 12. P. 123505. DOI: 10.1063/1.2940130.
79. **Chekalin S. V., Mel'nikov A. A., Misochko O. V.** Ultrafast coherent lattice and incoherent carrier dynamics in bismuth: time-domain results. *Laser Phys.* 2014. V. 24. N 9. P. 094004. DOI: 10.1088/1054-660X/24/9/094004.
80. **Ischenko A. A., Aseyev S. A.** Time Resolved Electron Diffraction: for chemistry, biology and material science. San Diego: Elsevier. 2014. 310 p.
81. **Bugayev A., Esmail A., Abdel-Fattah M., Elsayed-Ali H. E.** Coherent phonons in bismuth film observed by ultrafast electron diffraction. *AIP Advances*. 2011. V. 1. N 1. P. 012117. DOI: 10.1063/1.3574888.
82. **Moriena G., Hada M., Sciaini G., Matsuo J., Dwayne Miller R. J.** Femtosecond electron diffraction: Preparation and characterization of (110)-oriented bismuth films. *J. Appl. Phys.* 2012. V. 111. N 4. P. 043504. DOI: 10.1063/1.3684975.
83. **Sokolowski-Tinten K., Li R. K., Reid A. H., Weathersby S. P., Quirin F., Chase T., Coffee R., Corbett J., Fry A., Hartmann N., Hast C., Hettel R., Horn von Hoegen M., Janoschka D., Lewandowski J. R., Ligges M., Meyer zu Heringdorf F., Shen X., Vecchione T., Witt C., Wu J., Dürr H. A., Wang X. J.** Thickness-dependent electron–lattice equilibration in laser-excited thin bismuth films. *New J. Phys.* 2015. V. 17. N 11. P. 113047. DOI: 10.1088/1367-2630/17/11/113047.

69. **Raman R. K., Murooka Y., Ruan C.-Y., Yang T., Berber S., Tománek D.** Direct Observation of Optically Induced Transient Structures in Graphite Using Ultrafast Electron Crystallography. *Phys. Rev. Lett.* 2008. V. 101. N 7. P. 077401. DOI: 10.1103/PhysRevLett.101.077401.
70. **Touloukian Y. S., Kirby R. K., Taylor R. E., Desai P. D.** Thermal expansion: Metallic elements and alloys. Boston, MA: Springer US. 1975. 1440 p.
71. **Buffat P., Borel J. P.** Size effect on the melting temperature of gold particles. *Phys. Rev. A*. 1976. V. 13. N 6. P. 2287-2298. DOI: 10.1103/PhysRevA.13.2287.
72. **Wang N., Rokhlin S. I., Farson D. F.** Nonhomogeneous surface premelting of Au nanoparticles. *Nanotechnology*. 2008. V. 19. N 41. P. 415701. DOI: 10.1088/0957-4484/19/41/415701.
73. **Billinge S. J. L., Levin I.** The Problem with Determining Atomic Structure at the Nanoscale. *Science*. 2007. V. 316. N 5824. P. 561-565. DOI: 10.1126/science.1135080.
74. **McGreevy R. L.** Reverse Monte Carlo modelling. *J. Phys. Condens. Matter*. 2001. V. 13. N 46. P. R877-R913.
75. **Mironov B. N., Kompanets V. O., Aseev S. A., Ishchenko A. A., Misochko O. V., Chekalin S. V., Ryabov E. A.** Direct observation of the generation of coherent optical phonons in thin antimony films by the femtosecond electron diffraction method. *JETP Letters*. 2016. V. 103. N 8. P. 531-534. DOI: 10.1134/s0021364016080099.
76. **Mel'nikov A.A., Misochko O.V., Chekalin S.V.** Investigation of coherent phonons in bismuth by femtosecond laser and X-ray pulse probing. *JETP Letters*. 2009. V. 89. N 3. P. 129-132. DOI: 10.1134/s0021364009030072.
77. **Misochko O. V., Ishioka K., Hase M., Kitajima M.** Fully symmetric and doubly degenerate coherent phonons in semimetals at low temperature and high excitation: similarities and differences. *J. Phys. Condens. Matter*. 2006. V. 18. N 47. P. 10571-10584.
78. **Ishioka K., Kitajima M., Misochko O. V.** Coherent A1g and Eg phonons of antimony. *J. Appl. Phys.* 2008. V. 103. N 12. P. 123505. DOI: 10.1063/1.2940130.
79. **Chekalin S. V., Mel'nikov A. A., Misochko O. V.** Ultrafast coherent lattice and incoherent carrier dynamics in bismuth: time-domain results. *Laser Phys.* 2014. V. 24. N 9. P. 094004. DOI: 10.1088/1054-660X/24/9/094004.
80. **Ischenko A. A., Aseyev S. A.** Time Resolved Electron Diffraction: for chemistry, biology and material science. San Diego: Elsevier. 2014. 310 p.
81. **Bugayev A., Esmail A., Abdel-Fattah M., Elsayed-Ali H. E.** Coherent phonons in bismuth film observed by ultrafast electron diffraction. *AIP Advances*. 2011. V. 1. N 1. P. 012117. DOI: 10.1063/1.3574888.
82. **Moriena G., Hada M., Sciaini G., Matsuo J., Dwayne Miller R. J.** Femtosecond electron diffraction: Preparation and characterization of (110)-oriented bismuth films. *J. Appl. Phys.* 2012. V. 111. N 4. P. 043504. DOI: 10.1063/1.3684975.
83. **Sokolowski-Tinten K., Li R. K., Reid A. H., Weathersby S. P., Quirin F., Chase T., Coffee R., Corbett J., Fry A., Hartmann N., Hast C., Hettel R., Horn von Hoegen M., Janoschka D., Lewandowski J. R., Ligges M., Meyer zu Heringdorf F., Shen X., Vecchione T., Witt C., Wu J., Dürr H. A., Wang X. J.** Thickness-dependent electron–lattice equilibration in laser-excited thin bismuth films. *New J. Phys.* 2015. V. 17. N 11. P. 113047. DOI: 10.1088/1367-2630/17/11/113047.

84. **Streubühr C., Kalus A., Zhou P., Ligges M., Hanisch-Blicharski A., Kammler M., Bovensiepen U., Horn-von Hoegen M., von der Linde D.** Comparing ultrafast surface and bulk heating using time-resolved electron diffraction. *Appl. Phys. Lett.* 2014. V. 104. N 16. P. 161611. DOI: 10.1063/1.4872055.
85. **Davisson C. J., Germer L. H.** Reflection of Electrons by a Crystal of Nickel. *PNAS*. 1928. V. 14. N 4. P. 317-322.
86. **Thomson G. P., Reid A.** Diffraction of Cathode Rays by a Thin Film. *Nature*. 1927. V. 119. N P. 890. DOI: 10.1038/119890a0.
87. **Mark H., Wierl R.** Uber Electronenbeugung am Einzelnen Molekul *Naturwiss*. 1930. V. 18. N 9. P. 205.
88. **Murdick R. A., Raman R. K., Murooka Y., Ruan C.-Y.** Photovoltage dynamics of the hydroxylated Si(111) surface investigated by ultrafast electron diffraction. *Phys. Rev. B*. 2008. V. 77. N 24. P. 245329. DOI: 10.1103/PhysRevB.77.245329.
89. **Wang W., Lee T., Reed M. A.** Electron tunnelling in self-assembled monolayers. *Rep. Prog. Phys.* 2005. V. 68. N 3. P. 523-544.

84. **Streubühr C., Kalus A., Zhou P., Ligges M., Hanisch-Blicharski A., Kammler M., Bovensiepen U., Horn-von Hoegen M., von der Linde D.** Comparing ultrafast surface and bulk heating using time-resolved electron diffraction. *Appl. Phys. Lett.* 2014. V. 104. N 16. P. 161611. DOI: 10.1063/1.4872055.
85. **Davisson C. J., Germer L. H.** Reflection of Electrons by a Crystal of Nickel. *PNAS*. 1928. V. 14. N 4. P. 317-322.
86. **Thomson G. P., Reid A.** Diffraction of Cathode Rays by a Thin Film. *Nature*. 1927. V. 119. N P. 890. DOI: 10.1038/119890a0.
87. **Mark H., Wierl R.** Uber Electronenbeugung am Einzelnen Molekul *Naturwiss*. 1930. V. 18. N 9. P. 205.
88. **Murdick R. A., Raman R. K., Murooka Y., Ruan C.-Y.** Photovoltage dynamics of the hydroxylated Si(111) surface investigated by ultrafast electron diffraction. *Phys. Rev. B*. 2008. V. 77. N 24. P. 245329. DOI: 10.1103/PhysRevB.77.245329.
89. **Wang W., Lee T., Reed M. A.** Electron tunnelling in self-assembled monolayers. *Rep. Prog. Phys.* 2005. V. 68. N 3. P. 523-544.

Поступила в редакцию 10.04.2017
Принята к опубликованию 30.05.2017

Received 10.04.2017
Accepted 30.05.2017